Characterization of fluidized nanoparticle agglomerates by using adhesive CFD-DEM simulation

Daoyin Liu[1,2], Berend G. M. van Wachem[3], Robert F. Mudde[2], Xiaoping Chen[1], J. Ruud van Ommen[2]*

* Corresponding author. E-mail address: j.r.vanommen@tudelft.nl

1 Key Laboratory of Energy Thermal Conversion and Control of Ministry of Education, School of Energy and Environment, Southeast University, Nanjing 210096, Jiangsu, China

2 Department of Chemical Engineering, Faculty of Applied Sciences, Delft University of Technology, Julianalaan 136, 2628 BL Delft, The Netherlands

3 Thermofluids Division, Department of Mechanical Engineering, Imperial College London, Exibition Road, London SW7 2AZ, United Kingdom

Abstract

Nanoparticles form multi-stage agglomerates when they are fluidized: simple agglomerates (a few dozens of micrometres), and complex agglomerates (a few hundreds of micrometres). This paper studies nanoparticle fluidization by using adhesive CFD-DEM (Discrete Element Model) simulation, which includes an adhesive contact model having the ability to model the contact and bounce/stick between elastic-plastic and cohesive particles. The discrete elements represent the simple agglomerates of nanoparticles. The effects of particle density, fluidizing gas velocity, and van der Waals force on gas-solid flow and agglomerate behaviors are investigated. It is shown that the particles, representing simple agglomerates, form large agglomerates during fluidized process. As the agglomerates move around in the bed, they continuously break and recombine. The solid movement is evaluated by a dispersion coefficient and it decreases with increase in cohesion. By monitoring the evolution of contacts, the agglomerate breakage is visualized and compared for the different conditions. Increasing fluidizing gas velocity and reducing particle adhesion both increase agglomerate breakage rate. The structure parameters of agglomerates are further analyzed: averaged coordination number of agglomerates around 3.0, packing fraction around 0.2-0.3, and fractal dimension around 1.9-2.3, which can be used to indicate structures and formation mechanisms of agglomerates.

Keywords: Nanoparticle Fluidization; Agglomerate; Discrete Element Model; Adhesion

1. Introduction

Nanoparticle fluidization is a promising technique to disperse and process nanoparticles [1-4]. Extensive experimental studies have been performed on nanoparticle fluidization[1, 5]. Two aspects are of key importance: fluidization behavior and agglomerate structure, since nanoparticles are not fluidized individually but rather as large, very porous agglomerates.

To characterize the fluidization behavior, the minimum fluidization velocity (u_{mf}) and bed expansion ratio (h/h_{mf}) are usually used for measuring macro fluidization quality [6-9]. The reduction of cohesive forces or the increase of separating forces can result in a reduced u_{mf}, usually along with an increased h/h_{mf}. For example, u_{mf} (TiO_2) > u_{mf} (SiO_2), since the van der Waals forces (vdW) are larger for materials with higher surface energy [7]. u_{mf} can be reduced by pre-treatment of the anti-static surfactant, drying, or providing particles with an apolar coating, because of reduced cohesive forces (electrostatic force, capillary force, or hydrogen bond force) [7, 10]. Also, u_{mf} can be reduced by fluidization assistance methods including mechanical vibration, auxiliary magnetic fields, and ultrasound fields, because of increased separating forces [8, 11-13].

Regarding the agglomerate structure, information including the agglomerate size and fractal dimension, are investigated. It is generally accepted that the complex agglomerates are around a few hundreds of micrometres [6, 14, 15]. The fractal dimension can be used to characterize agglomerates, but its variation with various parameters still needs more investigations [16]. The agglomerate information can be obtained in different ways, but it remains difficult to obtain the agglomerate properties in-line [17].

The numerical simulations have also been used for studying nanoparticle fluidization. In order to make the following description consistent, we restate the concept of "agglomerate" here. In most studies, the commercial metaloxide nanopowders are considered, with primary particle sizes of 5-50 nm. Fluidized agglomerates of such materials have a multi-stage structure: aggregates of nanoparticles sintered during production (~200 nm), simple agglomerates (a few dozens of micrometres), and complex agglomerates (a few hundreds of micrometres) [6, 7, 18]. In literature, most of the simulation studies consider the complex agglomerates as 'particles' with the equivalent sizes and densities. The

simulations can predict bubbling dynamics and bed pressure expansion [19-21]. However, the model cannot reveal the structure dynamics of the complex agglomerates, e.g. breakage and reunion, which are also critical for the overall gas-solid contact efficiency. In our previous study [22], we have developed an adhesive CFD-DEM model, where the simple agglomerates are assumed as 'particles', which are the building blocks of the larger complex agglomerates. It is shown that this model can reveal agglomerate breakage and reunion, as well as fluidized dynamics. In that paper [22], we have presented details of the model and tested its reliability for studying fluidization; the fluidized bed undergoes uniform fluidization to defluidization by increasing the cohesive force.

In this study, the gas and solid flow dynamics, the agglomerate break-up and reunion behaviors, and the statistics of agglomerate properties (coordination number, packing fraction, fractal dimension) are investigated. The effect of particle density, cohesion, and fluidizing gas velocity are also compared. Through this effort, our aim is to show that the current adhesive CFD-DEM model is able to study the dynamic properties of the complex agglomerates as well as the fluidization behaviors.

2. Numerical Model

2.1 Adhesive CFD-DEM model

The adhesive CFD-DEM model is used for simulating nanoparticle agglomerate fluidization. The simple agglomerates are represented by cohesive and plastic particles. Since the model details are presented in our previous paper [22], only a general description is given here. The current adhesive CFD-DEM model is a combination of the conventional CFD-DEM model, an adhesive contact model, and a drag force scale method. The simulation is performed using MultiFlow, a parallel multi-phase flow solver [23]. The general algorithm at each time step is similar to the conventional CFD-DEM model, but the contact model is substituted by the adhesive contact model and the drag force is reduced by a scale factor. The governing equations with sub-models are summarized in Table 1.

Like the solver in the conventional CFD-DEM model, the motion of the gas phase is calculated by local averaged Navier-Stokes equations while the motion of each particle is calculated by Newton's second law. The interaction between the particles is modelled by the adhesive contact model. Basically, it is a hysteresis linear spring–dashpot contact model, which has the ability to model

different collision regimes, from bounce to stick, between elastic-plastic and cohesive particles. The elastic-plastic property is expressed by a plasticity index (ψ_p) which indicates the ratio between the loading and the unloading spring stiffness, $\psi_p = 1 - k_{n,load}/k_{n,unload}$ [24]. The cohesive force is expressed by a non-dimensional Bond number, e.g. $Bo_{vdw} = F_{vdw,0}/mg$.

The interaction between the gas and particles is modelled by a semi-empirical drag model with the drag force scale factor (ξ). In the current simulation, Wen&Yu drag force correlation is used [25, 26]. ξ is used to consider drag reduction when particles are agglomerated, an approach coming from simulation studies of Geldart A particles [27-29]. When particles are agglomerated, the particles inside the agglomerate hardly experience the gas flow, which results in a reduction of the inter-phase surface and thus the drag force. However, the accurate calculation of ξ is still an unresolved problem. In the previous study [22], we determined different values of ξ for cases with Bo_{vdw}= 0, 20, 50, and 100 by a "predictor-corrector method". It is shown that ξ= 0.2 is reasonable for Bo_{vdw}= 20 case. In this study, since the simulation conditions are close to Bo_{vdw}= 20, ξ= 0.2 is used as constant for all cases for simplification.

Table 1

2.2 Computational Setup

Simulations are performed on a three-dimensional fluidized bed with size of [4, 0.8, 20] mm, which contains particles representing the simple agglomerates. The fluidizing gas is air at room temperature, with density 1.205 kg/m^3 and viscosity 1.8e-5 kg/(m.s). At the inlet the uniform gas velocity is specified, and at the outlet the gas pressure–outlet boundary condition is adopted. At the walls, the no–slip wall condition for the gas phase is used. Considering the bed size is limited, the interaction between particles and wall is treated by noncohesive collision.

Based on experimental measurements, the size of the simple agglomerates is usually around 5–45 μm [18]. To avoid too heavy computation [30], the particle diameter (d_{sa}) is chosen as 40 μm to

represent the simple agglomerates. For the particle density (ρ_{sa}), we have compared two values, e.g. the heavy one, $\rho_{sa} = 250\,\mathrm{kg}/m^3$ estimabed based on simple agglomerates of TiO_2 nanoparticles, and the light one, $\rho_{sa} = 137\,\mathrm{kg}/m^3$ agglomerates of SiO_2.

The effect of vdW force is studied by changing Bo_{vdw}. In our previous study [22], Bo_{vdw} is changed from 0 to 100 for TiO_2 agglomerates, representing the vdW force 0–8 nN, which is based on literature study. The cases with $Bo_{vdw} = 0$ and 20 show uniform and agglomerating fluidization, but for the cases with Bo_{vdw} = 50 and 100, the bed makes the transition to a fixed bed regime. Thus, in this study the range of Bo_{vdw} is narrowed and varied from 5 to 20. Other input parameters of the contact model are kept constant: coefficient of restitution due to the visco-elastic nature e_{vis}= 0.8, frictional coefficient μ_f = 0.35, unloading spring stiffness $k_{n,unload}$ = 2 N/m, plasticity index ψ_p = 0.2, cohesive forces due to physical or chemical adsorption $F_{bond,0} = 0$ [22]. The Young's modulus of the agglomerates is a function of porosity, primary particles and surface energy, and estimated around the order of 100 KPa for the nanoparticle agglomerates [31]. Correspondingly, the stiffness is around the order of 1 N/m in the linear spring contact model. The kinetic energy dissipation due to plastic deformation of the nanoparticle agglomerates is mainly varied between 0.2 and 0.5, according to measurements by the nanoindentation [24]. The effect of fluidizing gas velocity (u_g) is also studied. Since the experimental studies in literature usually cover u_g from ~1 cm/s up to a few cm/s and minimum fluidization velocity (u_{mf}) is reported around or below 1 cm/s. In the current simulation, u_g is changed from 2 to 4 cm/s.

In a summary, the effects of particle density, fluidizing gas velocity, and vdW force are investigated. The simulation cases are summarized in Table 2. Cases 1 to 3 are used to study effect of u_g on fluidization with light particle agglomerates, Cases 4 to 6 to study effect of u_g on fluidization with heavy particle agglomerates, and Cases 6 to 8 to study effect of Bo_{vdw} on fluidization.

Table 2

2.3 Definition of agglomerate characteristics

The DEM particles, representing the simple agglomerates, will build larger complex agglomerates when fluidized. The complex agglomerate radius, coordination number, packing fraction, and fractal dimension are evaluated. Their definitions are listed in the following.

The agglomerate radius (R_{agg}) is defined by $m_{agg}R_{agg}^2 = \sum_1^{n_p} m_{sai}l_i^2$, where n_p is the particle number contained in an agglomerate, m_{agg} and m_{sa} the agglomerate mass and particle mass, and l_i the distance between the centers of the particle i and the agglomerate [32].

The packing fraction (p) is defined as the ratio between the sum of the particles' volume and the agglomerate's volume [33]. The coordination number (C_N) is defined as the number of touching neighbors for a given particle [33]. The fractal dimension (D_f) describes the relation between the agglomerate size and the agglomerate density and is determined from the equation $n_p = \left(R_{agg}/r_{sa}\right)^{D_f}$ [34].

2.4 Identification of agglomerates

The identification of agglomerates is not trivial in a dense particle system, since the short-term contacts (collisions) and long-term contacts (agglomeration) should be distinguished. In our previous paper, the DEM particles in contact whose relative velocity is smaller than a certain limit and coordination number larger than 2, are recognized as agglomerates, but the limit of the velocity could influence the results and should be chosen carefully [22]. In this paper, we identify the agglomerates by monitoring the breakage of contacts. If a contact holds for a given period of time, then it is treated as an agglomerate. The longer time period allows to identify more stable agglomerates. This method is more objective, but the computation is expensive. There are other criteria could be possible for agglomerate identification by image analysis methods. An evaluation of various criteria is beneficial and currently ongoing in our group. We will now briefly describe the agglomerate identification procedure for this paper:

Step 1, Choose the reference time (t_0), and one comparison time (t_1). The contacts at t_0 and t_1 are compared, and the shared particles are considered as candidates of agglomerate's elements and stored as a list.

Step 2, Build the agglomerates from the shared contact list. The particles in the shared list of t_0 and t_1 are linked using a Last In First Out (LIFO) data structure. For example, if particle A contacts with B1, B2 and B3, B1 again contacts with C1 and C2, and B2 again contacts with D1, then the agglomerate is built in the sequence of A-B1-C1-C2-B2-D1-B3.

Step 3, Choose another comparison time (t_2), and repeat Steps 1 and 2.

Therefore, by choosing a reference time t_0 and a series of comparison times, the evolution of agglomerate breakage can be obtained, as illustrated in Figure 1 for the case ρsa250vdw20ug4. The particles in the same agglomerate are shown with the same color. Here, the reference time is 1.00 s. Initially, at time 1.01 s, the agglomerates identified are very large, because the particles just touching briefly are included in agglomerates. With an increase in the time interval, the agglomerates gradually become smaller and the number of agglomerate decreases. In order to represent typical agglomerates, the agglomerates with only a few particles are filtered out. Here, we use 15 as the lower limit. The limit setting is like image analysis of agglomerates during experiment studies. It could change results quantitatively, but it does not change the trend of the effects of parameters on agglomerates breakage, because it influences equally to each of the case. In preliminary studies, we compared the limit values of 15 and 10, they give very similar quantitative results about agglomerate breakage rate and probability distribution of agglomerate properties.

The disappearance of agglomerates with time indicates that the 'old' agglomerates identified at t_0 completely break up. Thus, by monitoring the evolution of contacts, the stability of agglomerates can be characterized. This information cannot be obtained by examining contacts separately for each instantaneous image. Note that although the process of agglomerate recombination is not examined in this paper, the recombination and breakage of agglomerates maintain a dynamic equilibrium during normal fluidization.

Figure 1

3. Results

The simulation results include two aspects: flow pattern at the macro scale and agglomerate dynamic at the meso scale. In this paper, the flow pattern is described briefly to check the model's reliability and show the overall picture of fluidization. Prediction of agglomerate dynamic is the unique of the current model and thus it is focused.

3.1 General flow pattern

Figure 2 shows the instantaneous solid flow pattern for all the cases listed in Table 2. Generally, the particles are fluidized in the form of agglomerates. The agglomeration depends on particle density, fluidizing gas velocity and vdW force. A quantitative analysis of the agglomeration will be given in Sections 3.2 and 3.3. The dynamics of the solid flow patterns are shown by an animation in the supplementary materials of this paper. From Figure 2 and the supplementary animation, the dynamic breakage and reunion processes of the agglomerates can be observed. As the agglomerates move around in the bed, they break into smaller ones. Meanwhile the smaller ones recombine continuously to new, larger agglomerates.

Figure 3 shows the instantaneous gas velocity vector with contours of solid volume fraction for four of the cases. Only four cases are selected for shown, since the others give similar information. Generally, some channelling with higher gas velocity is observed. In the cases of ρsa137vdw20ug2 and ρsa250vdw5ug4, the distribution of solid and gas velocity is relatively more uniform, because of the weaker particle cohesion. Compared with the case ρsa250vdw20ug2, the channeling in the case ρsa250vdw20ug4 is more obvious, which indicates that channeling increases by increasing fluidizing gas velocity under the same particle cohesion.

Figure 4a shows the time-series of bed pressure drop (ΔP) for different cases. The solid straight lines indicate the ideal bed pressure drop calculated by the weight of bed materials per bed cross section area. It is shown that ΔP fluctuates around the theoretical values. The fluctuation amplitudes are expressed by the standard deviation ($\sigma_{\Delta p}$) of ΔP, as shown in Figure 4b. As expected, by increasing particle density, u_g from 2 cm/s to 4 cm/s, and Bo_{vdw} from 5 to 20, $\sigma_{\Delta p}$ increases.

Figure 2

Figure 3

Figure 4a

Figure 4b

In order to quantify the particle movement, the solid dispersion coefficient is calculated based on statistics of particle displacement [35-37]. Given trajectory of a single particle, the local solid dispersion (D_n) of particle n can be calculated as following

$$D_n = \frac{(\Delta r_n)^2}{2\Delta t} \quad (1)$$

where Δr_n is the displacement of particle n during a time interval Δt. The displacement can be along horizontal or vertical direction. The averaged solid dispersion coefficient (D_s) is calculated by

$$D_s = \frac{1}{N}\sum_{n=1}^{N}\frac{(\Delta r_n)^2}{2\,\Delta t} = \frac{1}{\Delta t}\frac{1}{N}\sum_{n=1}^{N}\frac{(\Delta r_n)^2}{2} = \frac{1}{\Delta t}S^2 \qquad n = 1,\ldots,N \quad (2)$$

where S^2 is the mean of the squared displacement of all the particles, and N the particle number. Based on the curve of $S^2 - \Delta t$, D_s is determined. As an example, Figure 5a shows the curve of $S^2 - \Delta t$ along z direction for four of the cases. It is shown that S^2 increases with time and then fluctuates around some steady value. The value of D_s is calculated from the maximal slope of the secant line from its initial time to a selected time.

Figure 5b summarizes D_s along x and z directions (D_{sx} and D_{sz}) for different cases. The $D_s$along y direction is not presented here, since it is much smaller as a result of the limited bed depth. It is shown that D_{sz} is much larger than D_{sx}, which means the vertical solids mixing is dominant. D_{sz} decreases by increasing particle density and particle cohesion, while D_{sz} increases obviously with increase in fluidizing gas velocity. It is interesting to note here that the qualitative trends of D_{sz} with the parameters are the same for the agglomerate breakage rate, which will be presented in the following section.

Figure 5a

Figure 5b

3.2 Agglomerate breakage

Before further analyzing the agglomerate breakage, we emphasize that the agglomerate breakage and reunion maintain a dynamic equilibrium. This point is proved by plotting the variation of the coordination number (C_N) with time. Figure 6a shows the averaged C_N with time, which is calculated by averaging C_N over all the particles at each instantaneous time. It is shown that C_N increases quickly from 0 to 2-3 within 0.3 seconds, and then fluctuates around one steady value, which indicates that the agglomerate breakage and recombination are in a dynamic balance.

Figure 6b shows the probability distribution of C_N for one selected case, ρsa250vdw20ug4, at different times. The distribution curve quickly becomes stable, with the range of C_N from 0 to 7. Again, the stable distribution of C_N indicates that the agglomerates breakage and reunion are balanced.

From Figures 6a and 6b, it is interesting to note that the averaged C_N is a bit larger than that of normal fluidized beds, which fluctuates around 1.7 in a fluidized bed with particle diameter of 100 μm (Figure 22 in Ref. [38]). Also, the distribution shape is very similar to the normal fluidized conditions, with dominant coordination ranging from 1 to 4, but there are some quantitative differences in frequency of accounts (Figure 18 in Ref. [38]).

Figure 6a

Figure 6b

The agglomerate breakage for different cases can be compared by both visualization and statistical methods. Figure 7 visualizes the agglomerate breakage by highlighting the evolution of one selected agglomerate. The particles in one agglomerate are tagged with the black color at time 1.01 s, and then traced in the following times. For a good visualization of the agglomerate breakage, here only 1/5 of the background particles are shown. It is clear that the case ρsa250vdw20ug2 shows the slowest agglomerate breakage rate, while the case ρsa250vdw5ug4 shows the fastest rate. Thus, increasing fluidizing gas velocity and decreasing particle adhesion both increase agglomerate breakage rate.

Figure 7a

Figure 7b

Figure 7c

Figure 7d

To quantitatively compare the agglomerate breakage rate of the different cases, the agglomerate number (N_{agg}) and agglomerate diameter (d_{agg}) are calculated during the evolution of contacts following the approach shown in Figure 1. Figure 8a compares N_{agg} as a function of time interval for the different cases. For the light particle cases, N_{agg} first decreases rapidly and then decreases gradually. The rapid decrease is caused by breakage of weak contacts, while the slow decrease is caused by breakage of stable contacts. By comparison of the two fractions, it can be seen that the fraction of the weak contacts is dominant.

For the heavy particle cases, the decrease of N_{agg} is slower, and becomes even slower by increasing the vdW force or decreasing u_g. Furthermore, it can be seen that N_{agg} first increases within a very short time. The increase in N_{agg} indicates a different breakage mechanism from that during the decrease period, which will be discussed in the following along with the variation of d_{agg}.

Figure 8b shows the mass-averaged d_{agg} as a function of time interval for the different cases. Generally, d_{agg} for the heavy particle cases are larger than light particle cases. For all the cases, during the evolution of contacts, d_{agg} first decreases rapidly, and then decreases gradually to a value around 0.2 mm. After some period with stable values, d_{agg} decreases to zero before the time interval reaching 1.5 s for most cases. However, d_{agg} stays intact for the case ρsa250vdw20ug2, which means the agglomerate is more stable. Again, it indicates that increasing particle cohesion or decreasing fluidizing gas velocity leads to decrease in agglomerate breakage rate.

The above different behaviors of N_{agg} and d_{agg} with agglomerate breakage are further analyzed. The process with an increase in N_{agg} but decrease in d_{agg}, is caused by agglomerate fragmentation,

i.e. one agglomerate breaks down into more agglomerates. As d_{agg} increases, it takes longer time for N_{agg} to reach maximum, which indicates the fragmentation lasts longer. This is because large agglomerates tend to fragment. However, the process with a decrease in both N_{agg} and d_{agg} is mostly a result of agglomerate attrition, i.e. the agglomerate becomes smaller by losing small fragments (i.e., one or a few DEM particles) from it. When this process continues, the agglomerate will become smaller and smaller, and is no longer counted when small enough (here the lower limit value N_{agg}=15).

Therefore, we can conclude that there are two kinds of breakage, i.e., fragmentation and attrition. Generally, the fragmentation leads to an increase in N_{agg} while the attrition leads to a decrease in N_{agg}. Also, there are different contacts in an agglomerate, i.e. weak contacts, strong contacts, and sometimes permanent contacts, which result in different stabilities of agglomerates.

Figure 8c compares critical times for different cases, which are determined from the data shown in Figures 8a and 8b. The critical times are τ_{Nmax}, τ_{N15}, and τ_{ds}, defined as the time when N_{agg} is maximum, N_{agg} less than 15, and d_{agg} becomes steady, respectively. By comparing τ_{Nmax}, τ_{N15}, and τ_{ds}, it is clear that the agglomerates break faster in case of light particles than for heavy particles. The characteristic times decrease by decreasing the particle cohesion and increasing the fluidizing gas velocity. It is note that the agglomerate breakage rate has the similar trend with the solids dispersion coefficient from the macro method.

Figure 8a

Figure 8b

Figure 8c

3.3 Agglomerate properties

In this section, statistical analysis is performed on the agglomerate properties. Figure 9 shows the mass-averaged d_{agg}, C_N, p, and D_f for different cases, at the three critical times of τ_{Nmax}, τ_{N15}, and τ_{ds}. Please note that the average C_N presented in Section 3.2 is for all the particles in the bed, while

here C_N is averaged only over particles in agglomerates. As time increases from τ_{Nmax} to τ_{N15}, decrease is found for d_{agg}, C_N and D_f of different cases and increase is found for p, which is a result of the evolution of the agglomerate breakage.

It is shown that C_N is around 3.0 and p around 0.2-0.3 for different cases. C_N and p can reflect agglomerate structure. Based on a review on the coordination [33], for the random loose packing of mono-sized spheres, C_N ranges from 4.4 to 6 and p from 0.55 to 0.62. Lower packing density and coordination are observed when surface forces are dominant. The minimal stability of agglomerates under gravity is 3.0 to 3.5 contacts and packing fraction of 0.30. Therefore, the agglomerates here are roughly close to the structure with minimal stability.

It is shown that D_f is around 1.9-2.3 and it is generally smaller for light particle cases than heavy particle cases. It is extensively reported by experimental studies that the fluidized nanoparticle agglomerates have D_f about 2 [16]. A low D_f usually indicates open cluster structure. The formation of agglomerates by particle-cluster and cluster–cluster agglomeration mechanisms leads to large difference of D_f. For example, agglomerates made by diffusion-limited cluster-cluster agglomeration (DLCA) and ballistic cluster–cluster agglomeration (BCCA) are open clusters, with D_f = 1.8 and D_f = 1.9, while agglomerates made by diffusion-limited particle–cluster agglomeration (DLA) and ballistic particle–cluster agglomeration (BPCA) are dense clusters, with D_f= 2.5 and D_f = 3.0 [39]. Therefore, the fluidized agglomerates have a dominant BCCA or DLCA formation mechanism. Figure 10 shows the probability distribution of d_{agg}, C_N, p, and D_f for one selected case, ρsa250vdw20ug4, at times of τ_{Nmax}, τ_{N15}, and τ_{ds}. It is shown that the distribution ranges of these properties are not wide. The combination of the parameters of d_{agg}, C_N, p and D_f characterizes the agglomerate structure, which can highly affect gas diffusion within the agglomerate; this is a very important parameter when carrying out gas phase reactions on the primary particle surface within the agglomerate. A combination of simulation and experimental validation is a useful tool for getting more insight in the behaviour of fluidized nanoparticle agglomerates.

Figure 9a

Figure 9b

Figure 9c

Figure 9d

Figure 10

4. Discussion

In the above sections, we have demonstrated the adhesive CFD-DEM model can reveal properties of complex agglomerates during fluidization process. The probability distribution or the instantaneous evolution of agglomerate breakage-reunion can be directly explored. In future, quantitative validation of the model from the meso scale is required. The agglomerate structure reflected by the parameters, e.g. coordination, packing fraction, fractal dimension, can be compared with experimental measurements and used to improve understanding on fluidized nanoparticle agglomerates. Another unresovle problem, we point here again, is that how to calcualte the drag force reduction as a result of agglomeration. A presumed averaged scale factor used currently could be refined by considering agglomerate size and density locally but the computation will be very expensive.

From a broader view on modelling and understanding on nanoparticle fluidization, we should keep in mind that the current CFD-DEM model covers scales only from the simple agglomerates to the fluidized bed with size of a few millimeters. On the one hand, scale-up modelling of a fluidized bed with size of a few centimeters is encouraged for a direct comparison with experiments. On the other hand, micro simulation is encouraged to build relation among the scales of the primary nanoparticles, aggregates, and simple agglomerates. Towards this, a multi-scale modelling strategy will be developed for studying the relation between micromechanical nanoparticle properties and fluidization process.

5. Conclusions

Agglomerate dynamics are investigated in a nanoparticle fluidized bed with different particle density, cohesion, and fluidizing gas velocity, by using adhesive CFD-DEM simulation. The main conclusions that can be drawn from the simulations are:

(1) As the nanoparticle agglomerates move around in the bed, they break and recombine repeatedly. Gas channelling is observed in case of strong agglomeration.

(2) The averaged solid dispersion coefficient along bed height (D_{sz}) is much larger than that along bed width. D_{sz} increases with increasing fluidizing gas velocity, and decreases with increasing particle cohesion. A strong correlation is observed between the dispersion coefficient and the agglomerate breakage rate.

(3) The instantaneous coordination number averaged over all the particles in the bed is constant around 2~3 during fluidization, which is a bit larger than normal fluidized beds.

(4) The evolution of agglomerates are visualized and the agglomerate breakage is compared for different cases. Increasing fluidizing gas velocity or reducing particle adhesion can increase agglomerate breakage rate. Also, there are different contacts in an agglomerate, i.e. weak contacts, strong contacts, and sometimes permanent contacts, which result in different stabilities of agglomerates.

(5) Statistics of agglomerates show that, the averaged coordination number (C_N) is around 3.0, packing fraction (p) around 0.2-0.3, and fractal dimension (D_f) around 1.9-2.3. The combination of C_N and p indicates that the agglomerates are roughly close to the structure with minimal stability, while D_f indicates the agglomerates have a dominant BCCA or DLCA formation mechanism.

Finally, we point out improvements required by the current adhesive CFD-DEM model. We expect that the DEM model, together with the models of macro and micro scales, will be developed as a powerful tool for exploring relation between micromechanical nanoparticle properties and fluidization process.

Acknowledgments

We would like to acknowledge the financial supports for this study by the National Nature Science Foundation of China (51306035) and the ERC under the European Union's 7th Framework Programme (FP/2007-2013)/ERC Grant (279632). We thank Lilian de Martín for discussions on agglomerate identification.

Nomenclature

Roman symbols

Bo_{vdw}	Ratio of vdW force over particle gravity (-)
C_N	Coordination number (-)
D_f	Fractal dimension (-)
d_{agg}	Complex agglomerate diameter (mm)
d_{sa}	Simple agglomerate diameter (μm or mm)
D_{sx}	Solid dispersion coefficient along x axis (mm^2/s)
D_{sz}	Solid dispersion coefficient along z axis (mm^2/s)
h/h_{mf}	Bed expansion ratio (-)
m_{agg}	Complex agglomerate mass (g)
N_{agg}	Complex agglomerate number (-)
p	Packing fraction (-)
R_{agg}	Complex agglomerate radius (mm)
r_{sa}	Simple agglomerate radius (μm or mm)
u_g	Fluidizing gas velocity (cm/s)
u_{mf}	Minimum fluidization velocity (cm/s)

Greek symbols

ε_g	Bed voidage (-)
ψ_p	Plasticity index of simple agglomerate (-)
ξ	Drag force scale factor (-)
ρ_{sa}	Simple agglomerate density (kg/m^3)
ΔP	Bed pressure drop (Pa)
Δt	Time interval (s)
$\sigma_{\Delta p}$	Standard deviation of ΔP (Pa)
τ_{ds}	Critical time: when R_{agg} begins steady (s)
τ_{N15}	Critical time: when N_{agg} less than 15 (s)
τ_{Nmax}	Critical time: when N_{agg} maximum (s)

Acronyms

vdW	van der Waals force

Reference

[1] van Ommen JR, Valverde JM, Pfeffer R. Fluidization of nanopowders: a review. *Journal of Nanoparticle Research*, 2012, **14** (3): 737

[2] King DM, Liang X, Zhou Y, Carney CS, Hakim LF, Li P, Weimer AW. Atomic layer deposition of TiO2 films on particles in a fluidized bed reactor. *Powder Technology*, 2008, **183** (3): 356-363

[3] Wei F, Zhang Q, Qian W-Z, Yu H, Wang Y, Luo G-H, Xu G-H, Wang D-Z. The mass production of carbon nanotubes using a nano-agglomerate fluidized bed reactor: A multiscale space–time analysis. *Powder Technology*, 2008, **183** (1): 10-20

[4] Dasgupta K, Joshi JB, Banerjee S. Fluidized bed synthesis of carbon nanotubes - A review. *Chemical Engineering Journal*, 2011, **171** (3): 841-869

[5] Zhu X, Zhang Q, Wang Y, Wei F. Review on the nanoparticle fluidization science and technology. *Chinese Journal of Chemical Engineering*, 2016, **24** (1): 9-22

[6] Wang Y, Gu G, Wei F, Wu J. Fluidization and agglomerate structure of SiO2 nanoparticles. *Powder Technology*, 2002, **124** (1–2): 152-159

[7] Hakim LF, Portman JL, Casper MD, Weimer AW. Aggregation behavior of nanoparticles in fluidized beds. *Powder Technology*, 2005, **160** (3): 149-160
[8] Quevedo JA, Omosebi A, Pfeffer R. Fluidization enhancement of agglomerates of metal oxide nanopowders by microjets. *AIChE Journal*, 2010, **56** (6): 1456-1468
[9] Wang H, Zhou T, Yang JS, Wang JJ, Kage H, Mawatari Y. Model for calculation of agglomerate sizes of nanoparticles in a vibro-fluidized bed. *Chemical Engineering & Technology*, 2010, **33** (3): 388-394
[10] Tahmasebpoor M, de Martin L, Talebi M, Mostoufi N, van Ommen JR. The role of the hydrogen bond in dense nanoparticle-gas suspensions. *Physical Chemistry Chemical Physics*, 2013, **15** (16): 5788-5793
[11] Zhu C, Liu G, Yu Q, Pfeffer R, Dave RN, Nam CH. Sound assisted fluidization of nanoparticle agglomerates. *Powder Technology*, 2004, **141** (1–2): 119-123
[12] Valverde JM, Espin MJ, Quintanilla MAS, Castellanos A. Electrofluidized bed of silica nanoparticles. *Journal of Electrostatics*, 2009, **67** (2–3): 439-444
[13] Lepek D, Valverde JM, Pfeffer R, Dave RN. Enhanced nanofluidization by alternating electric fields. *AIChE Journal*, 2010, **56** (1): 54-65
[14] Valverde JM, Castellanos A. Fluidization, bubbling and jamming of nanoparticle agglomerates. *Chemical Engineering Science*, 2007, **62** (23): 6947-6956
[15] Wang XS, Rahman F, Rhodes MJ. Nanoparticle fluidization and Geldart's classification. *Chemical Engineering Science*, 2007, **62** (13): 3455-3461
[16] de Martín L, Fabre A, van Ommen JR. The fractal scaling of fluidized nanoparticle agglomerates. *Chemical Engineering Science*, 2014, **112**: 79-86
[17] de Martín L, Sanchez-Prieto J, Hernandez-Jimenez F, van Ommen JR. A settling tube to determine the terminal velocity and size distribution of fluidized nanoparticle agglomerates. *Journal of Nanoparticle Research*, 2013, **16** (1): 2183
[18] de Martín L, Bouwman WG, van Ommen JR. Multidimensional nature of fluidized nanoparticle agglomerates. *Langmuir*, 2014, **30** (42): 12696-12702
[19] Bahramian A, Ostadi H, Olazar M. Evaluation of drag models for predicting the fluidization behavior of silver oxide nanoparticle agglomerates in a fluidized bed. *Industrial & Engineering Chemistry Research*, 2013, **52** (22): 7569-7578
[20] Wang XS, Rahman F, Rhodes MJ. Application of discrete element method simulation for studying fluidization of nanoparticle agglomerates. *Canadian Journal of Chemical Engineering*, 2008, **86** (3): 514-522
[21] He Y, Lu H, Wen D, Ding Y. A numerical study on the gas fluidisation of secondary agglomerates of nanoparticles. *Progress in Natural Science*, 2005, **15**: 111-116
[22] Liu D, van Wachem BGM, Mudde RF, Chen X, van Ommen JR. An adhesive CFD-DEM model for simulating nanoparticle agglomerate fluidization. *AIChE Journal*, 2016, **62** (7): 2259-2270
[23] van Wachem BGM. MultiFlow, http://www.multiflow.org/. 2013,
[24] Schilde C, Kwade A. Measurement of the micromechanical properties of nanostructured aggregates via nanoindentation. *Journal of Materials Research*, 2012, **27** (4): 672-684
[25] Motlagh AHA, Grace JR, Salcudean M, Hrenya CM. New structure-based model for Eulerian simulation of hydrodynamics in gas–solid fluidized beds of Geldart group "A" particles. *Chemical Engineering Science*, 2014, **120**: 22-36
[26] van Wachem BGM, van der Schaaf J, Schouten JC, Krishna R, van den Bleek CM. Experimental validation of Lagrangian-Eulerian simulations of fluidized beds. *Powder Technology*, 2001, **116** (2-3): 155-165
[27] McKeen T, Pugsley T. Simulation and experimental validation of a freely bubbling bed of FCC catalyst. *Powder Technology*, 2003, **129** (1–3): 139-152
[28] van Wachem B, Sasic S. Derivation, simulation and validation of a cohesive particle flow CFD model. *AIChE Journal*, 2008, **54** (1): 9-19
[29] Wang J. A Review of Eulerian Simulation of Geldart A Particles in Gas-Fluidized Beds. *Industrial & Engineering Chemistry Research*, 2009, **48** (12): 5567-5577
[30] Berger KJ, Hrenya CM. Challenges of DEM: II. Wide particle size distributions. *Powder Technology*, 2014, **264** (0): 627-633
[31] Kendall K, Weihs TP. Adhesion of nanoparticles within spray dried agglomerates. *Journal of Physics D: Applied Physics*, 1992, **25** (1A): A3
[32] Eggersdorfer ML, Pratsinis SE. Agglomerates and aggregates of nanoparticles made in the gas phase. *Advanced Powder Technology*, 2014, **25** (1): 71-90
[33] Simons SJR, German RM. Coordination number changes during powder densification. *Powder Technology*, 2014, **253**: 368-376
[34] Bushell GC, Yan YD, Woodfield D, Raper J, Amal R. On techniques for the measurement of the mass fractal dimension of aggregates. *Advances in Colloid and Interface Science*, 2002, **95** (1): 1-50
[35] Liu DY, Chen XP. Lateral solids dispersion coefficient in large-scale fluidized beds. *Combustion and Flame*, 2010, **157** (11): 2116-2124

[36] Pallarès D, Johnsson F. A novel technique for particle tracking in cold 2-dimensional fluidized beds--simulating fuel dispersion. *Chemical Engineering Science*, 2006, **61** (8): 2710-2720
[37] Yang SL, Luo K, Qiu KZ, Fang MM, Fan JR. Coupled computational fluid dynamics and discrete element method study of the solid dispersion behavior in an internally circulating fluidized bed. *Industrial & Engineering Chemistry Research*, 2014, **53** (16): 6759-6772
[38] Hou QF, Zhou ZY, Yu AB. Micromechanical modeling and analysis of different flow regimes in gas fluidization. *Chemical Engineering Science*, 2012, **84** (0): 449-468
[39] Eggersdorfer ML, Pratsinis SE. The Structure of Agglomerates Consisting of Polydisperse Particles. *Aerosol Science and Technology*, 2012, **46** (3): 347-353

Figure Titles

Figure 1 Illustration of identification of agglomerates with increasing time intervals, for the case ρsa250vdw20ug4. The reference time is 1.00 s, and the comparison time is 1.01 s, 1.11 s, 1.21 s, 1.41 s, and 1.61 s, respectively. The particles in the same agglomerate are shown with the same color.

Figure 2 Solid flow pattern at 2.5 s for the different cases.

Figure 3 Gas velocity vectors with contours of solid volume fraction at 2.5 s. (a) case ρsa137vdw20ug2; (b) case ρsa250vdw20ug2; (c) case ρsa250vdw20ug4; (d) case ρsa250vdw5ug4

Figure 4 (a) Time-series and (b) time-averaged and standard deviation of bed pressure drop for the different cases.

Figure 5a Curve of squared displacement along vertical direction with time ($S^2 - \Delta t$) for four of the cases.

Figure 5b Averaged solid dispersion coefficient along the horizontal and vertical directions.

Figure 6a Averaged coordination number as a function of time for the different cases.

Figure 6b Probability distribution of coordination number for the case ρρsa250vdw20ug4 at different times.

Figure 7 Agglomerate breakage by tagging one agglomerate. (a) case ρsa137vdw20ug2; (b) case ρsa250vdw20ug2; (c) case ρsa250vdw20ug4; (d) case ρsa250vdw5ug4. The particles in one agglomerate are tagged with the black color at time 1.01 s, and then traced in the following times. For a good visualization of the agglomerate breakage, here only 1/5 of the background particles are shown.

Figure 8a Agglomerate number with time interval (Δt), by monitoring breakage of the contacts.

Figure 8b Mass-averaged agglomerate diameter with time interval (Δt), by monitoring breakage of the contacts.

Figure 8c Critical times determined from the curves of agglomerate number and agglomerate with the time interval.

Figure 9 (a) Mass-averaged agglomerate diameter, (b) coordination number, (c) packing fraction, and (d) fractal dimension for the different cases.

Figure 10 Probability distribution of agglomerate diameter, coordination number, packing density, and fractal dimension of case of ρsa250vdw20ug4.

Table Titles

Table 1 Governing equations and sub-models of the adhesive CFD-DEM model

Table 2 Simulation cases and description

Figure 1
Click here to download high resolution image

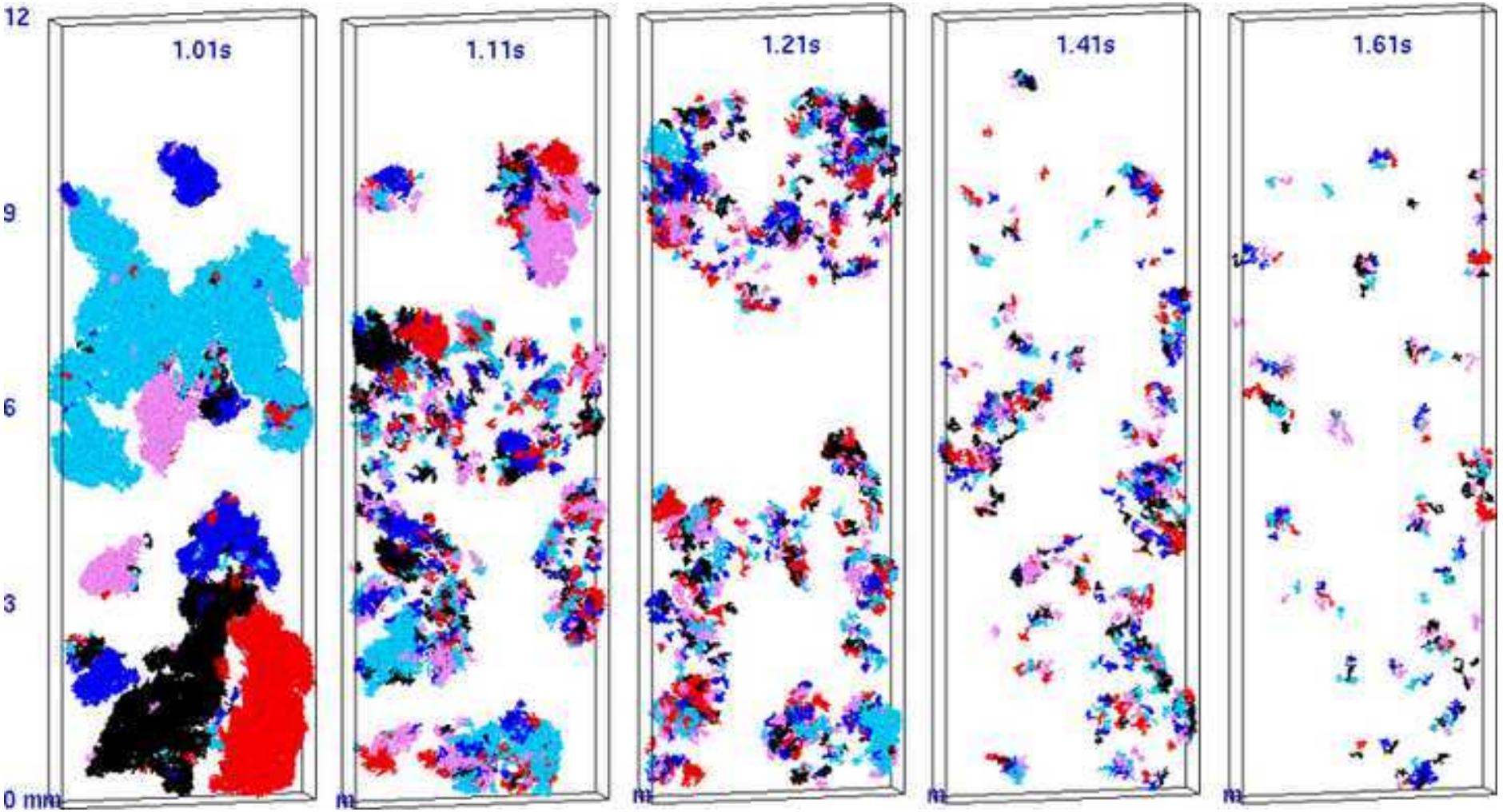

Figure 2

Click here to download high resolution image

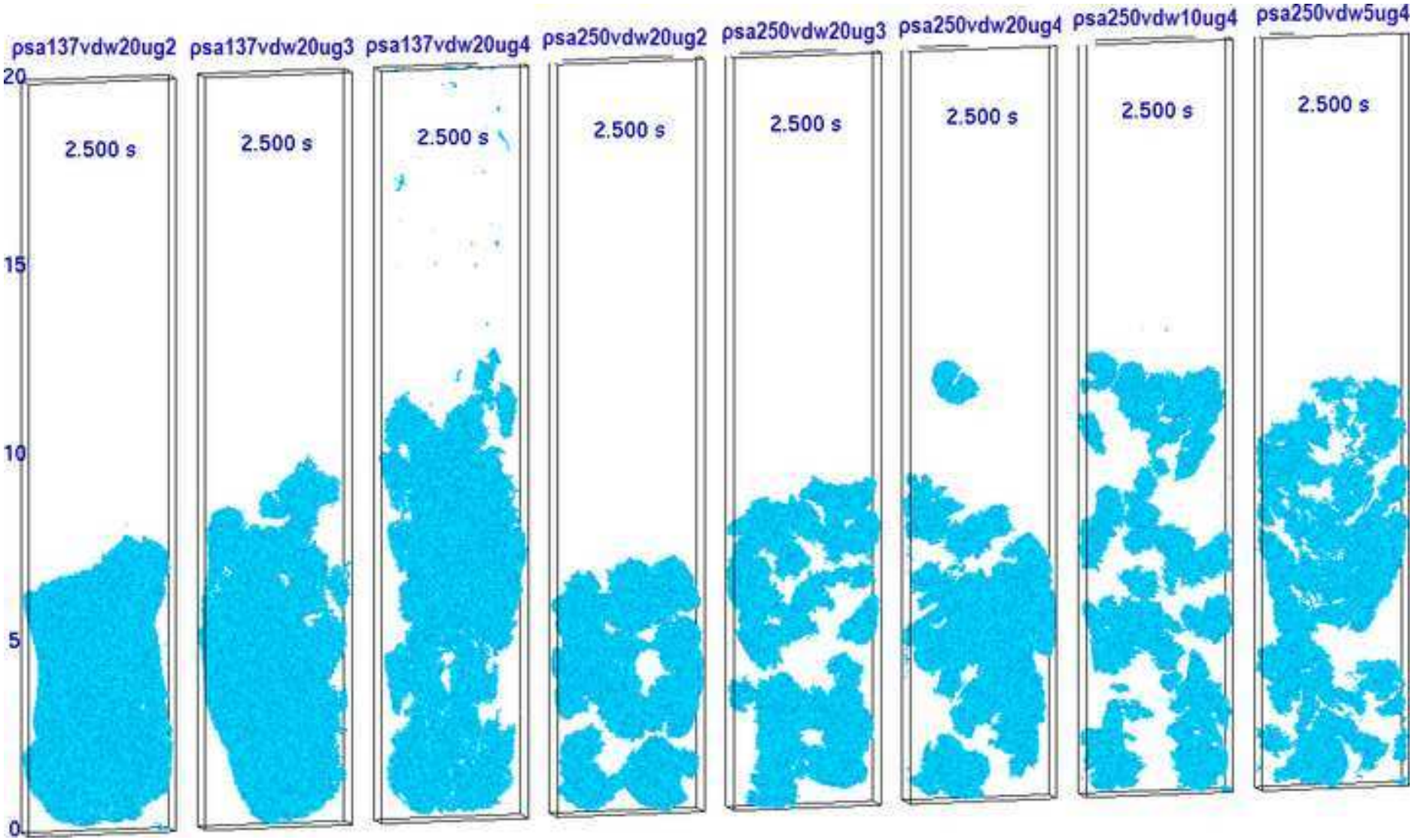

Figure 3
Click here to download high resolution image

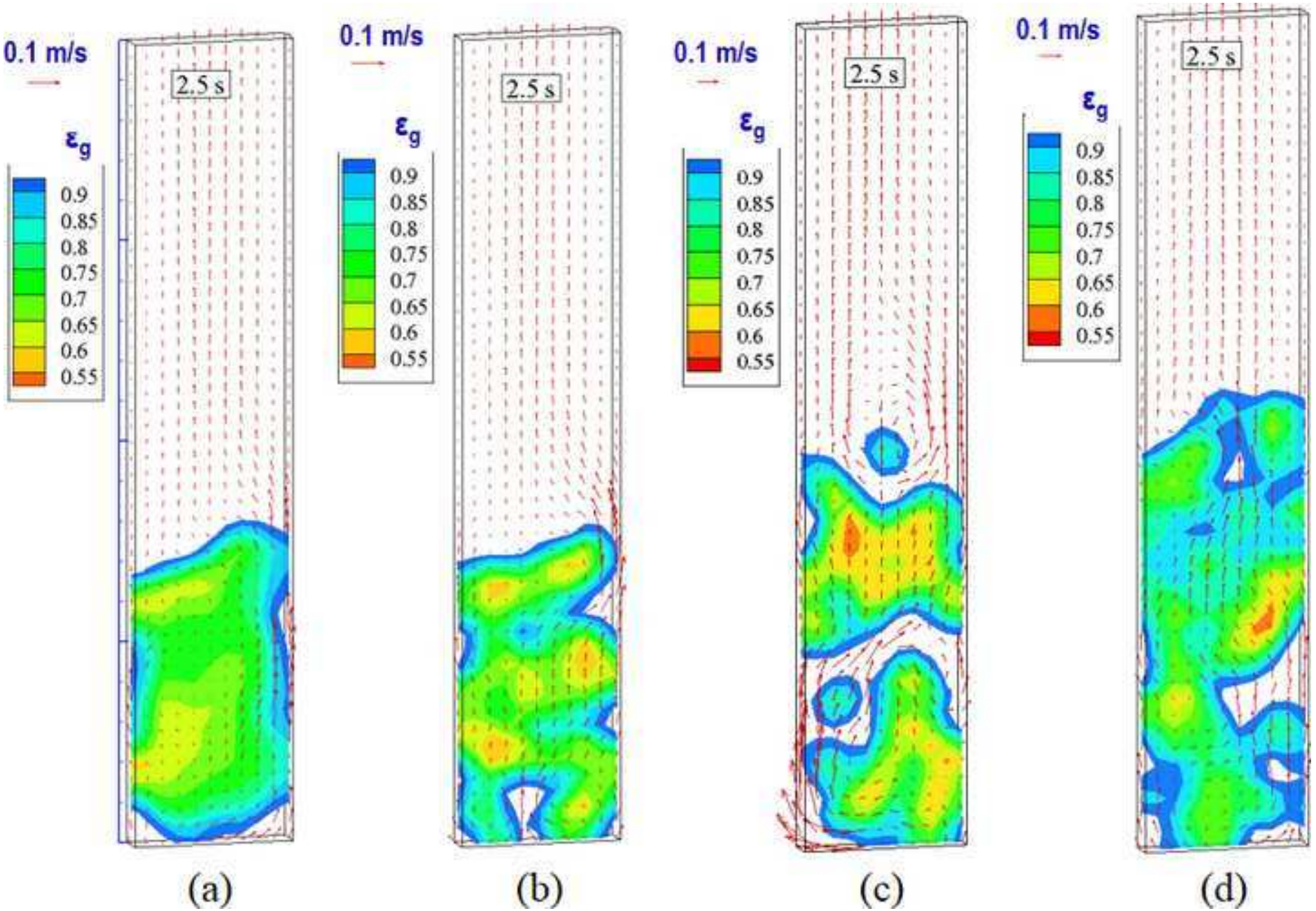

Figure 4a
Click here to download high resolution image

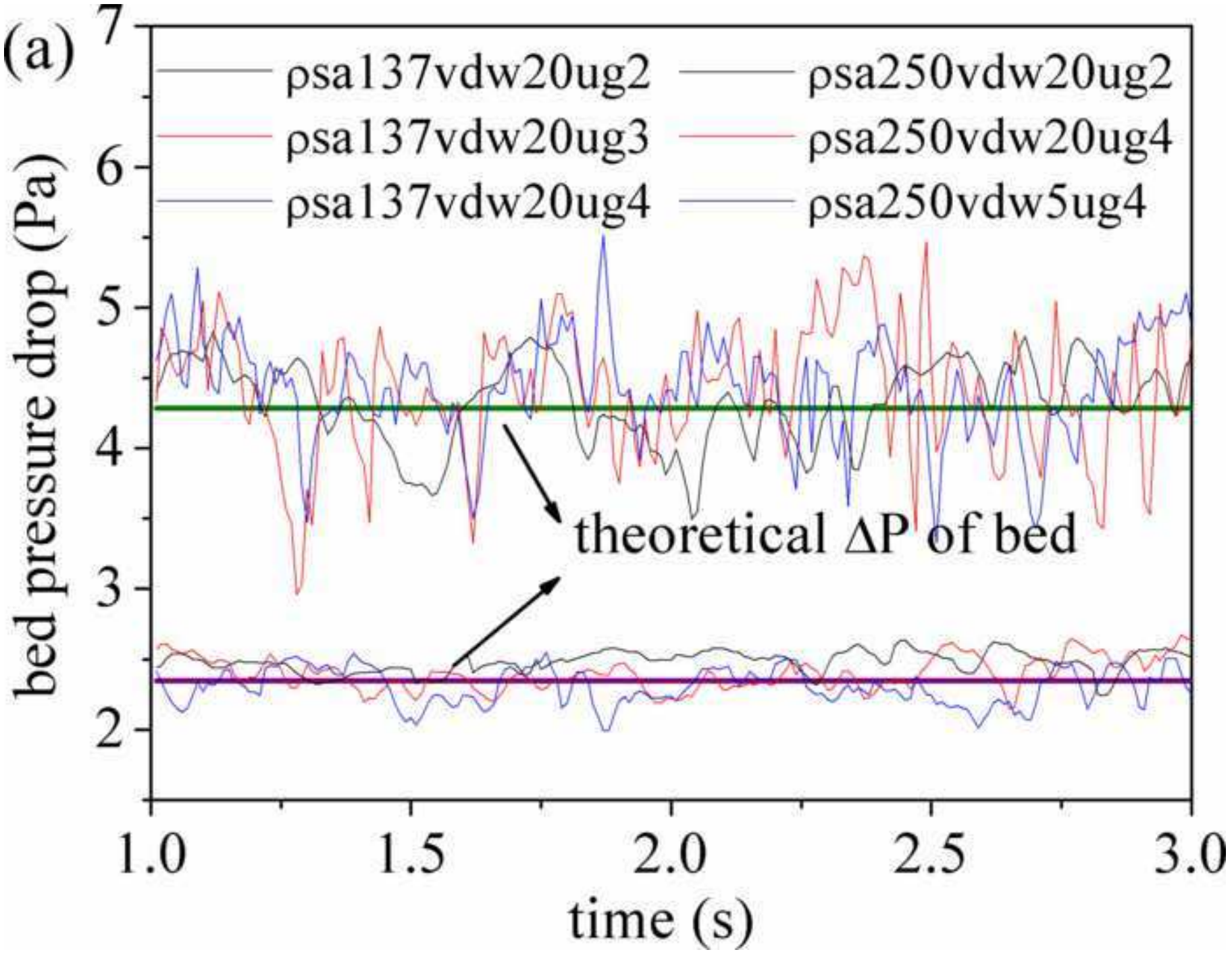

Figure 4b
Click here to download high resolution image

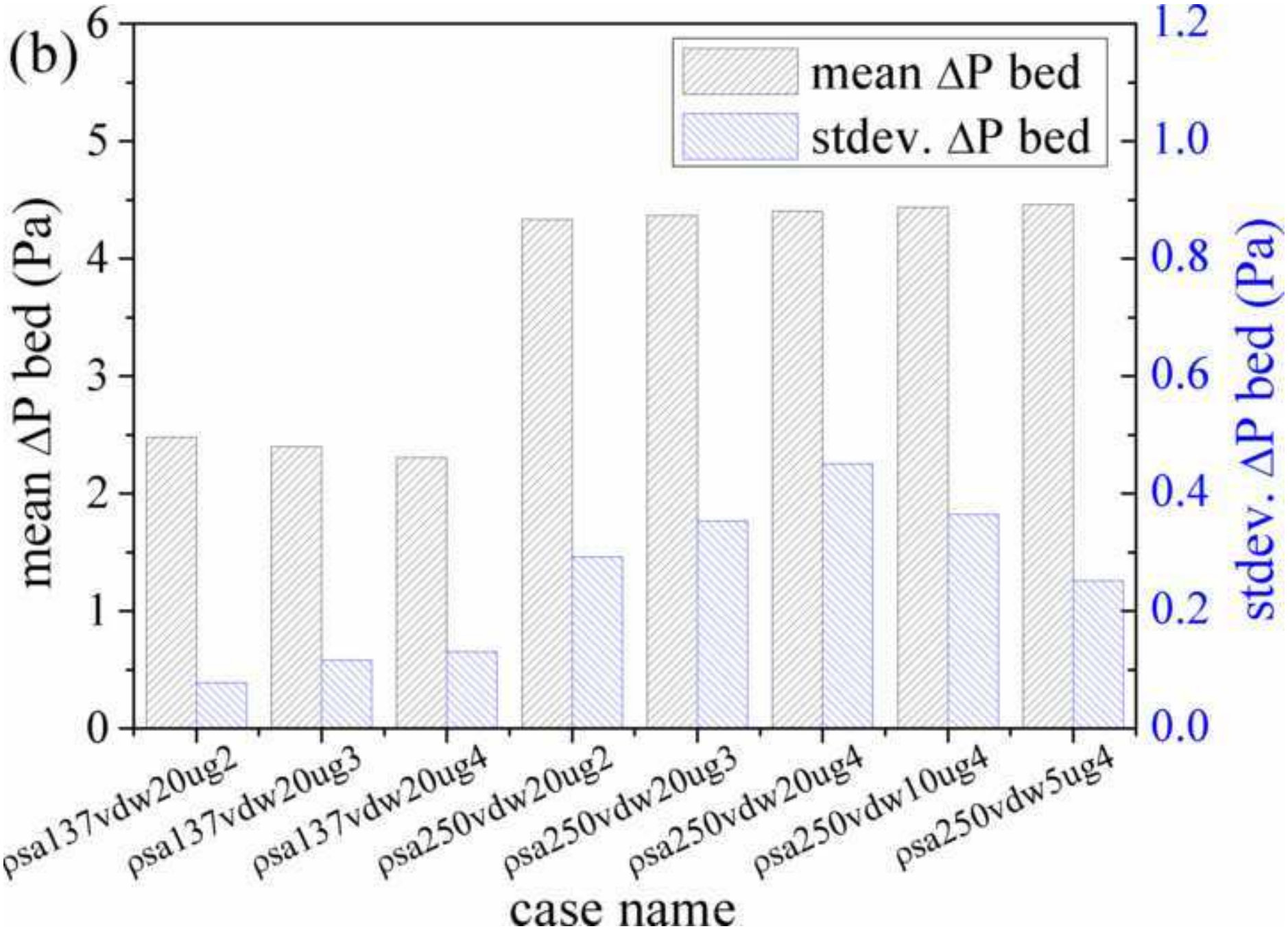

Figure 5a
Click here to download high resolution image

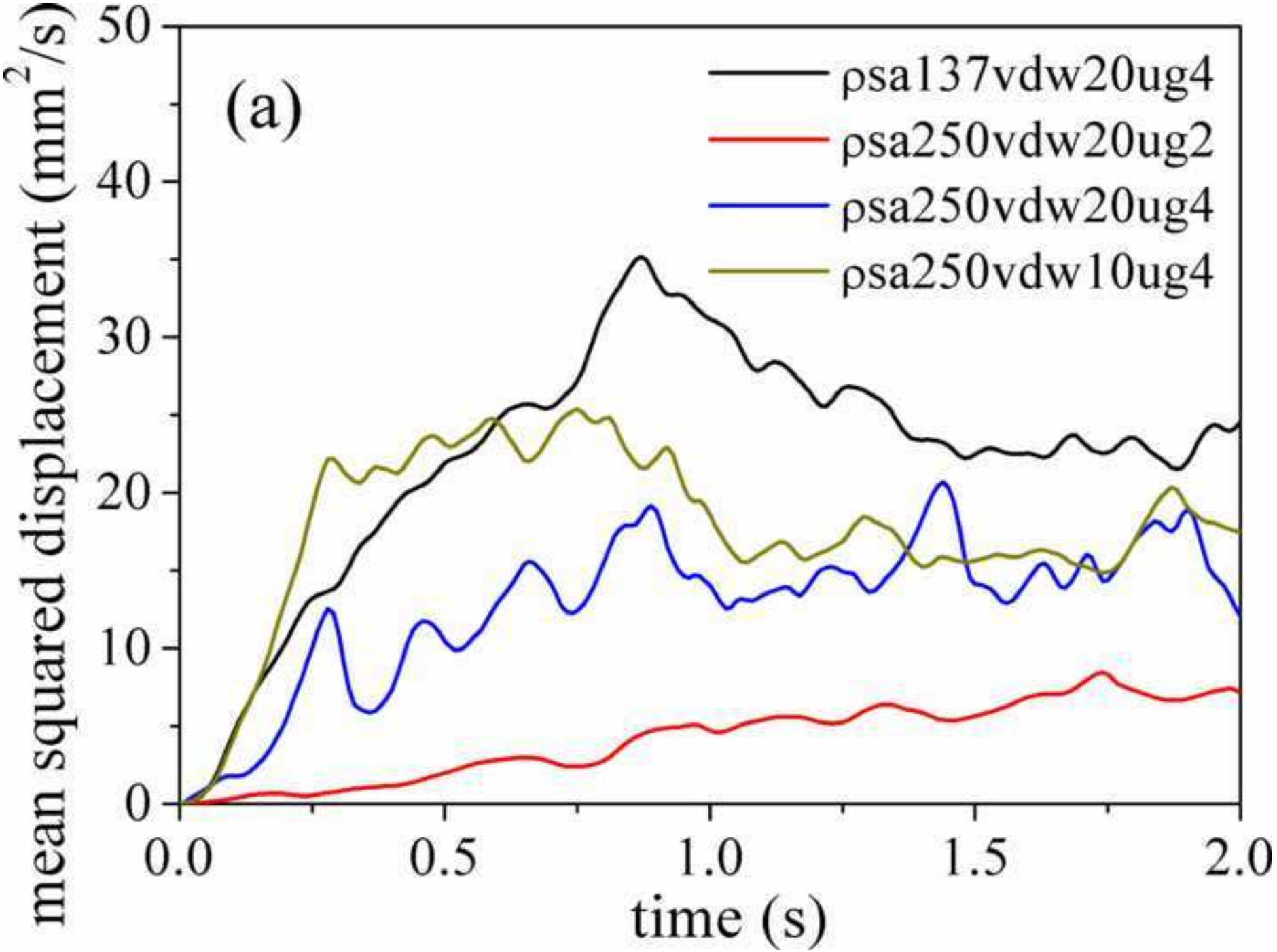

Figure 5b
Click here to download high resolution image

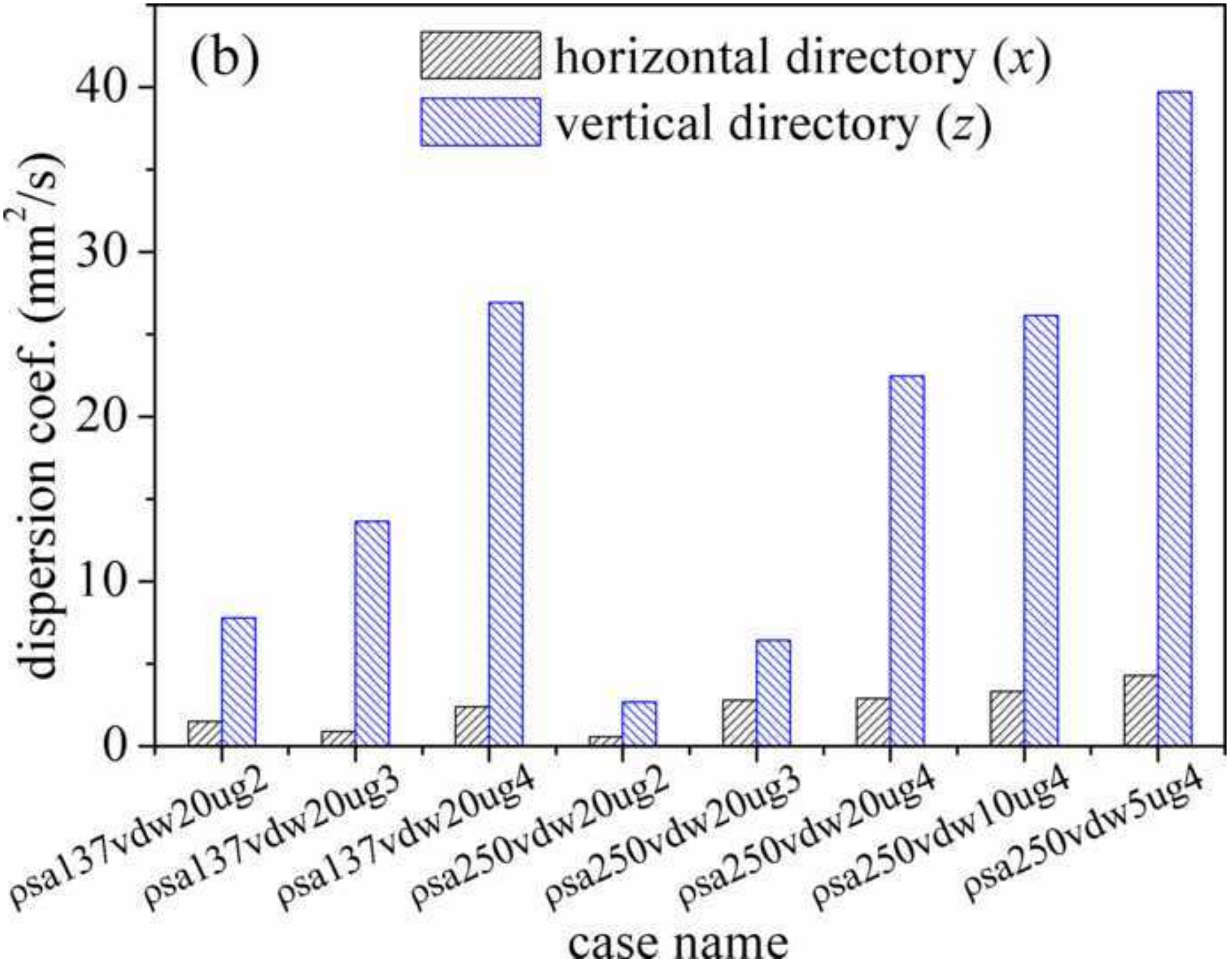

Figure 6a
Click here to download high resolution image

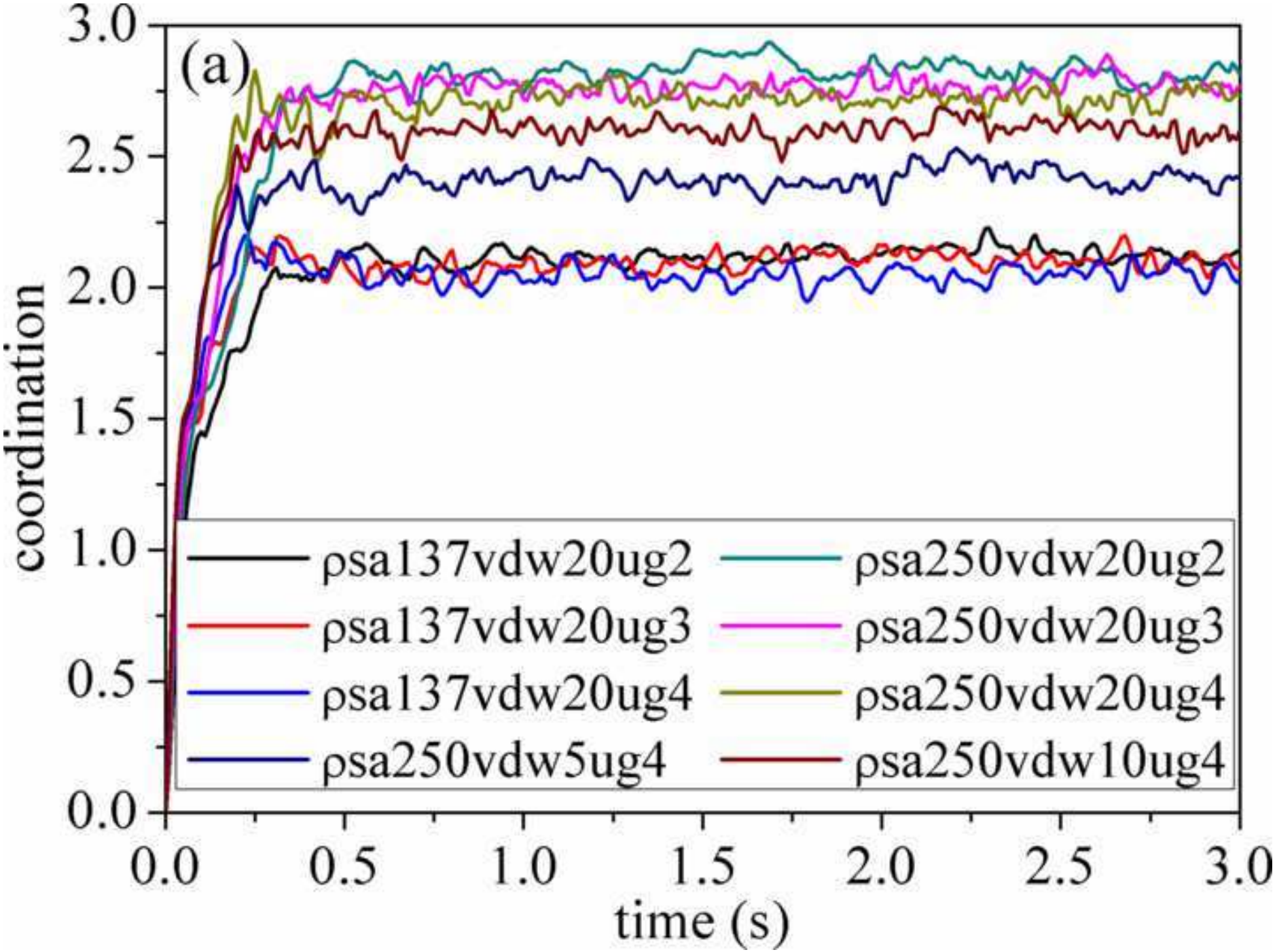

Figure 6b
Click here to download high resolution image

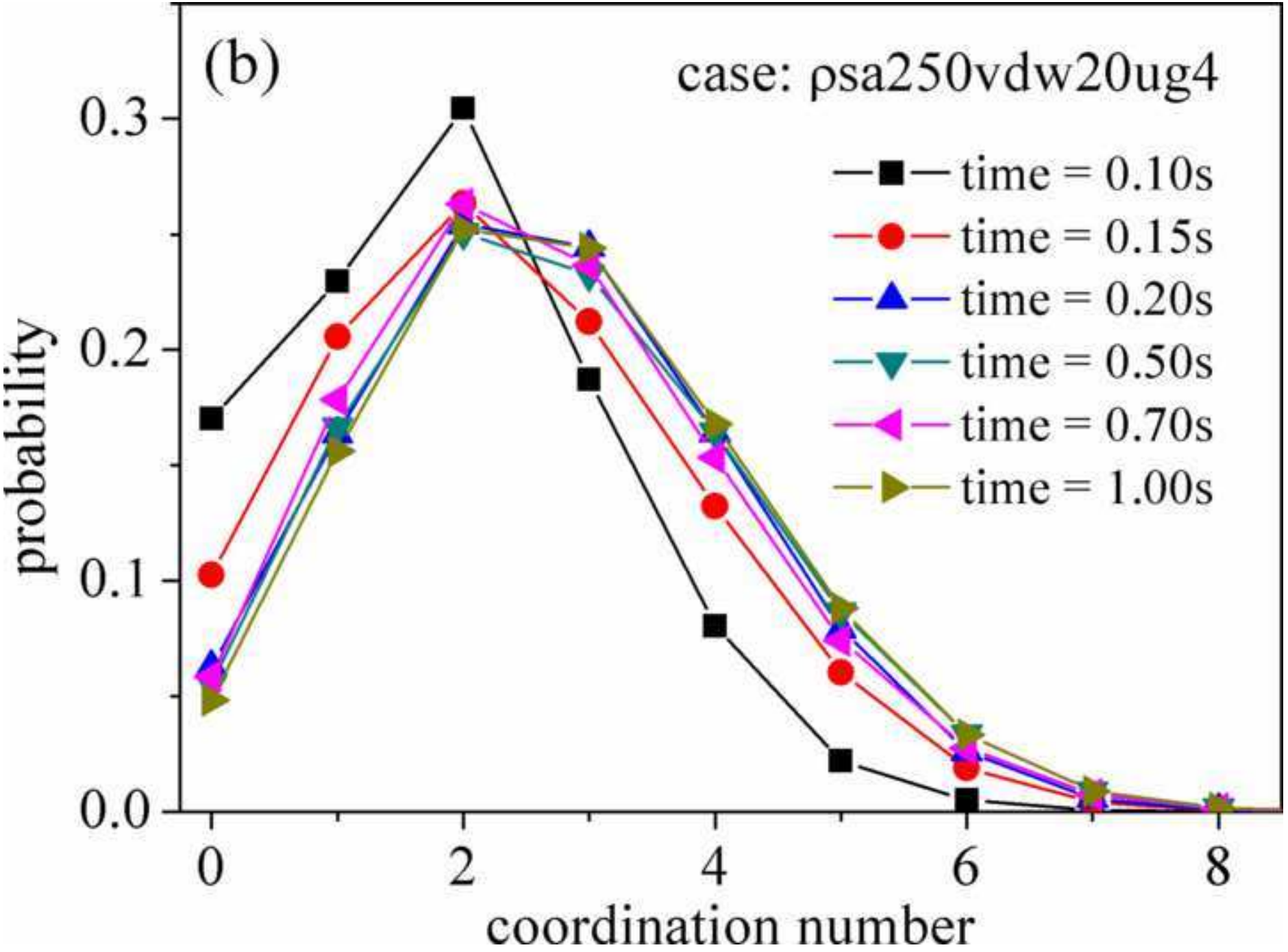

Figure 7a
Click here to download high resolution image

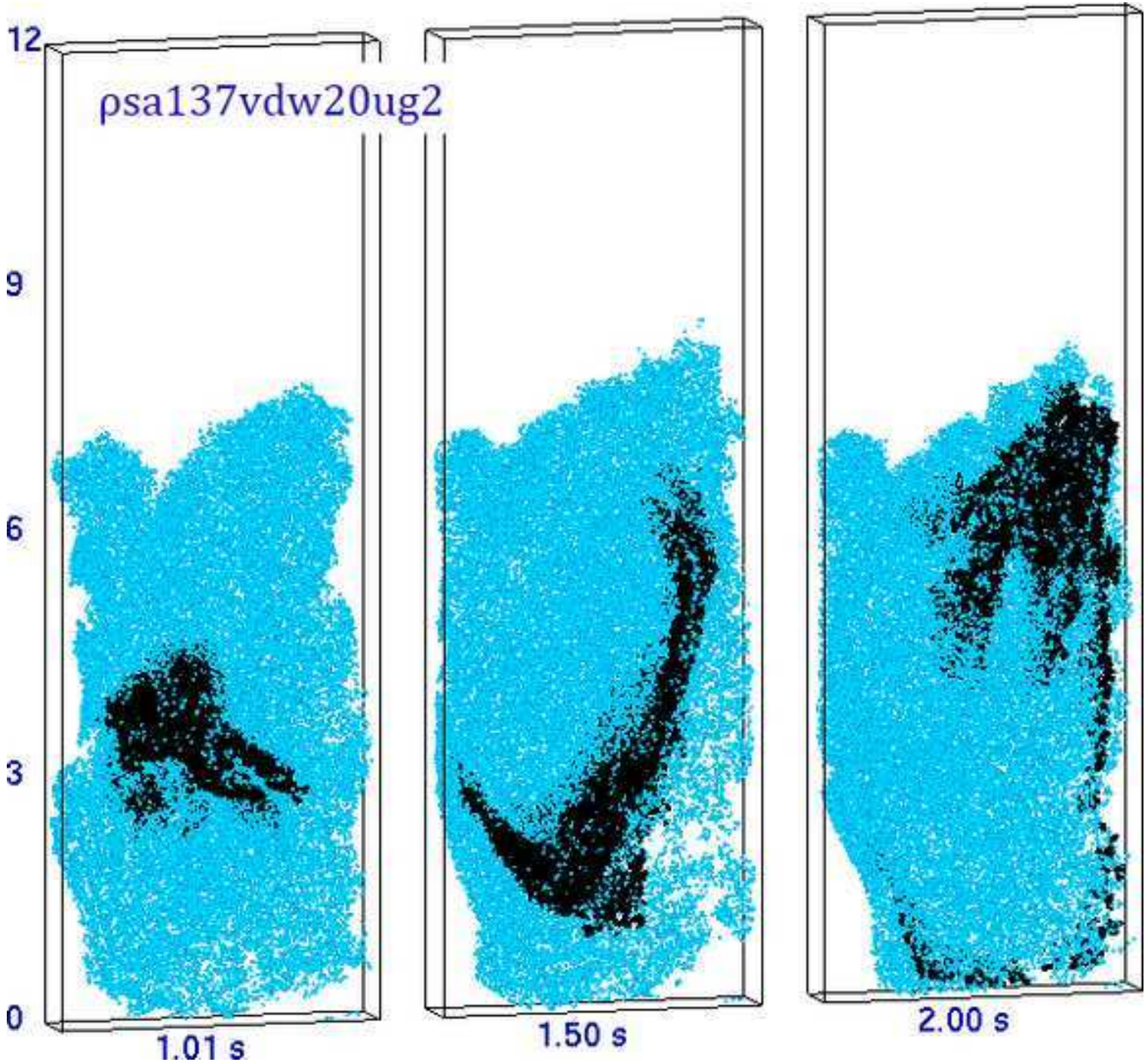

Figure 7b
Click here to download high resolution image

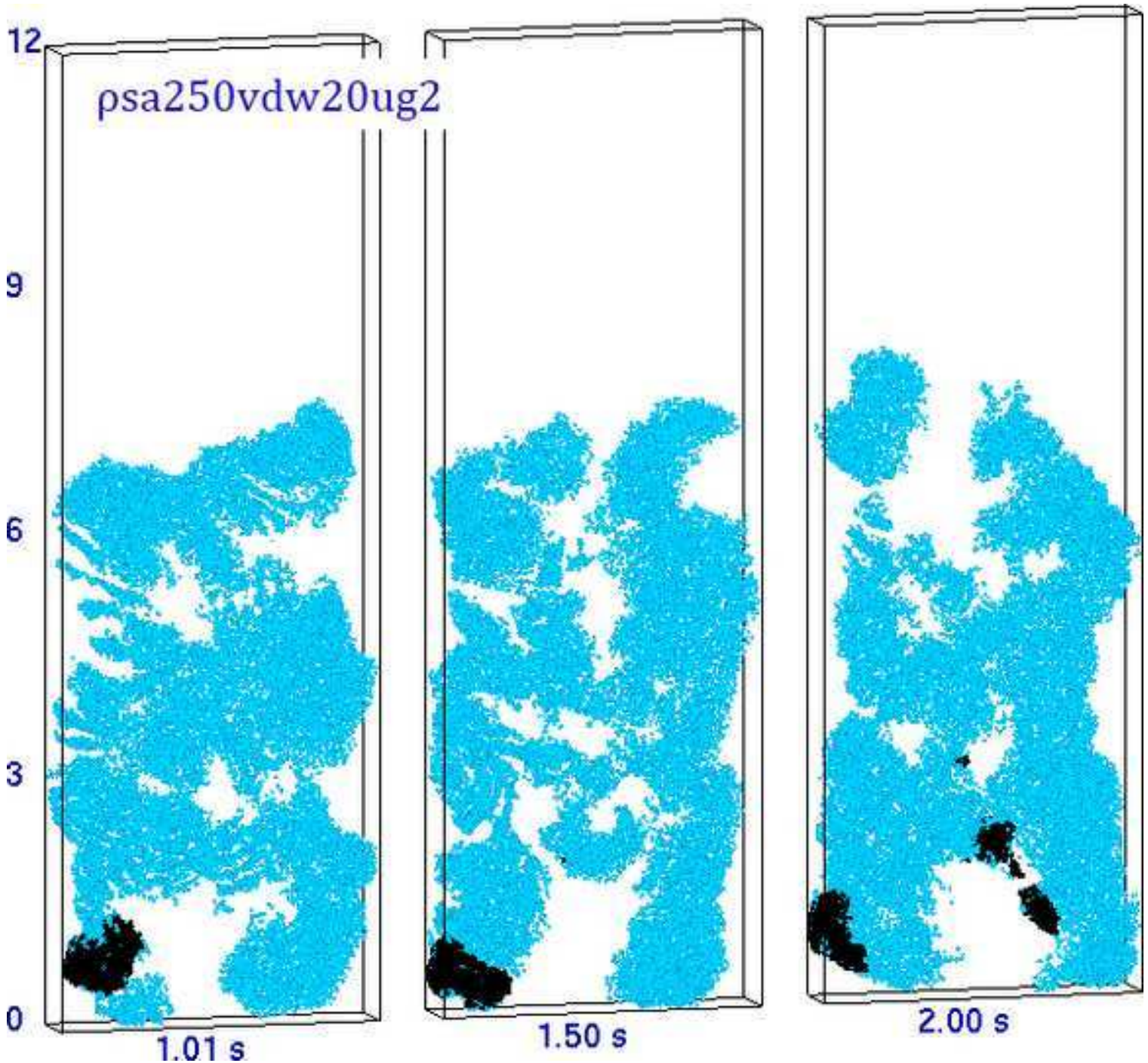

Figure 7c

Click here to download high resolution image

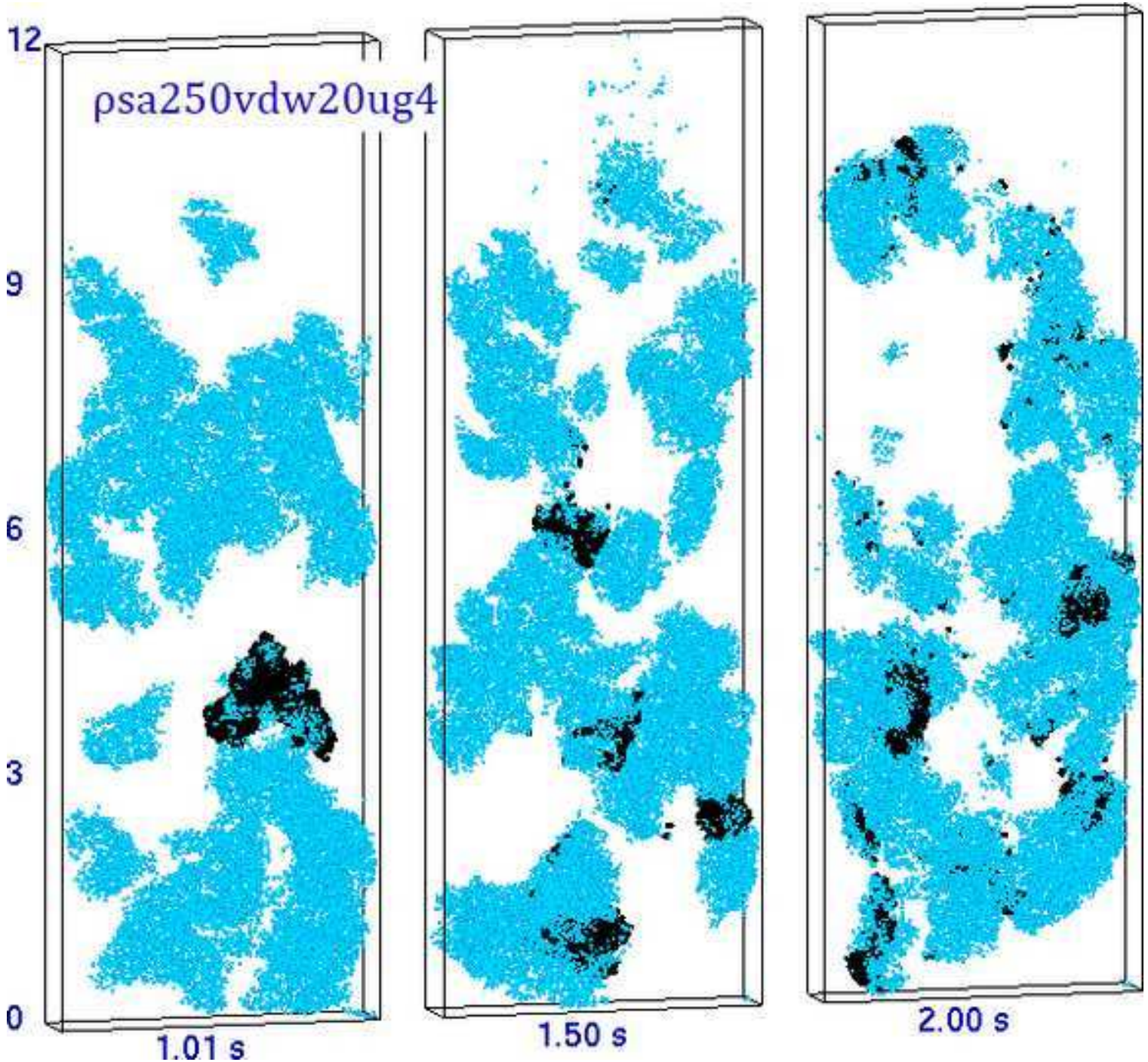

Figure 7d
Click here to download high resolution image

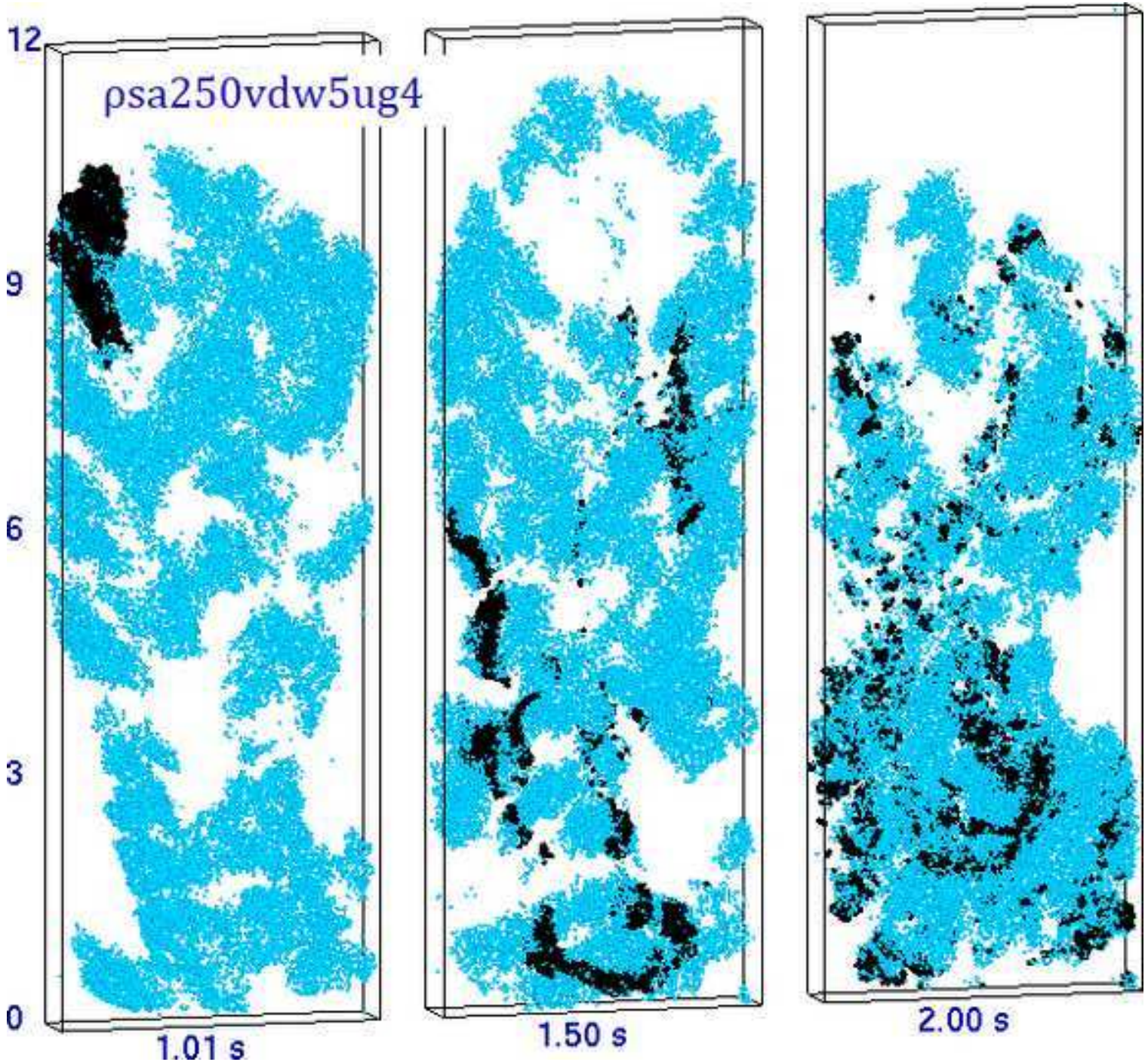

Figure 8a
Click here to download high resolution image

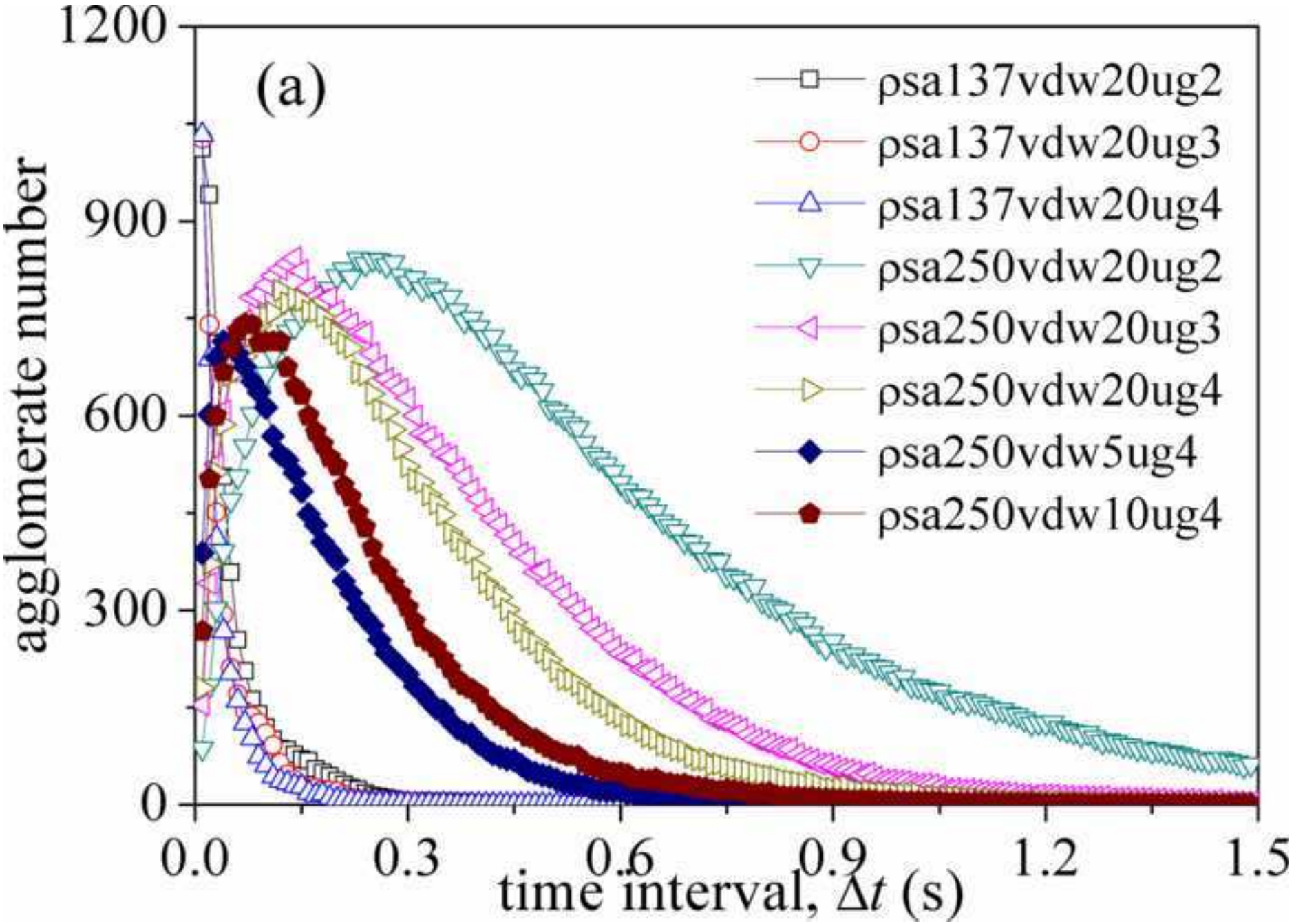

Figure 8b
Click here to download high resolution image

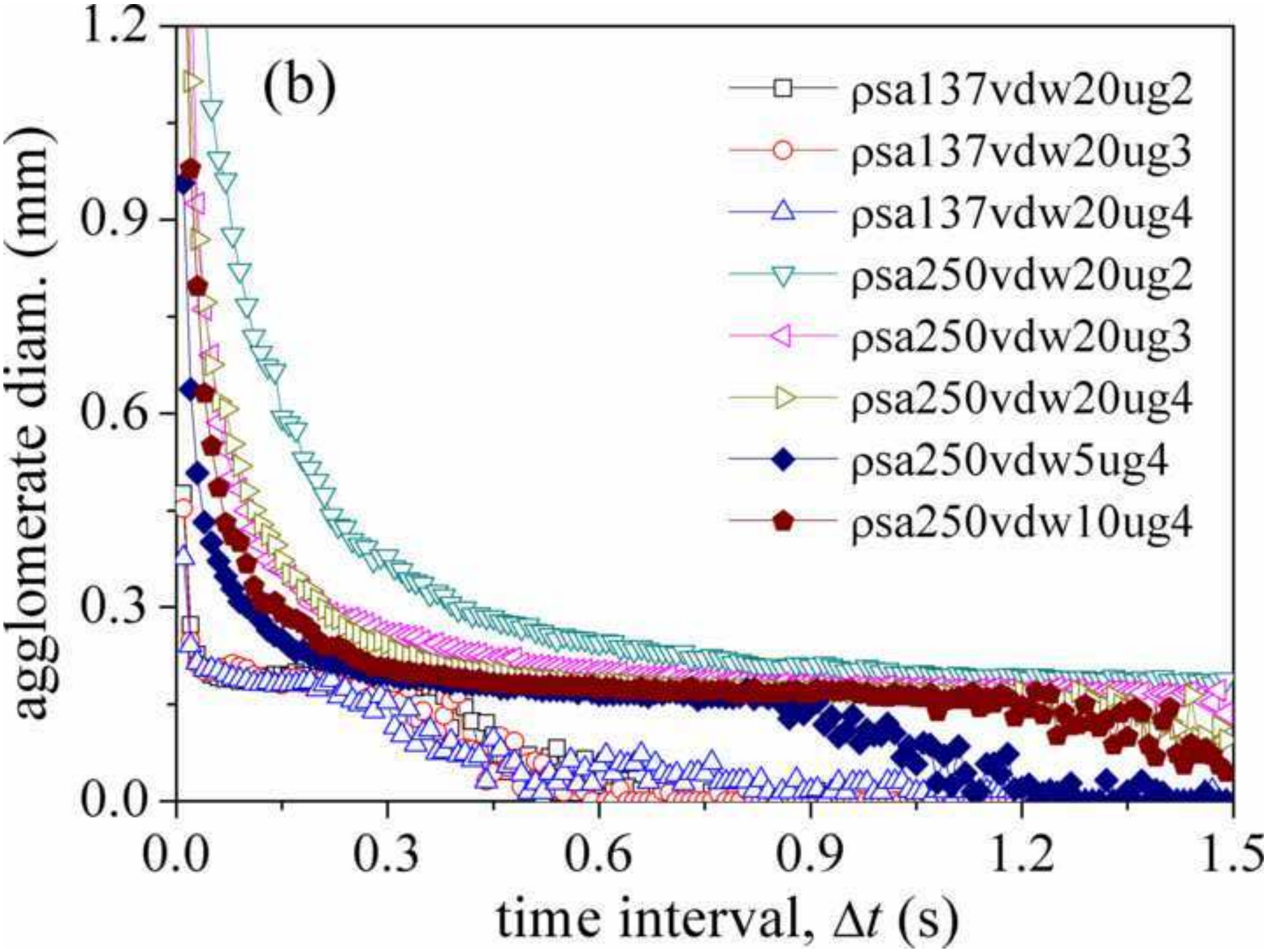

Figure 8c
Click here to download high resolution image

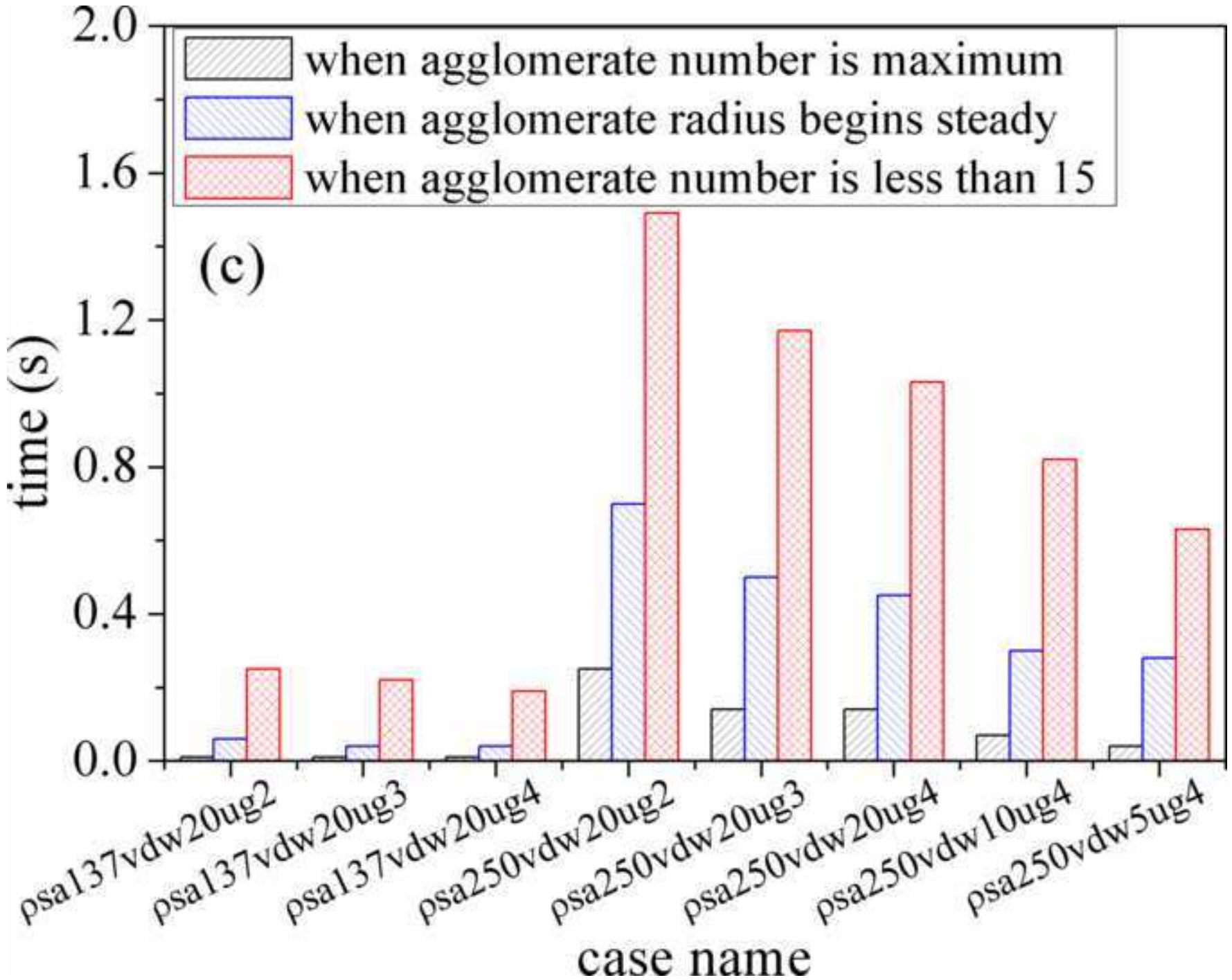

Figure 9a
Click here to download high resolution image

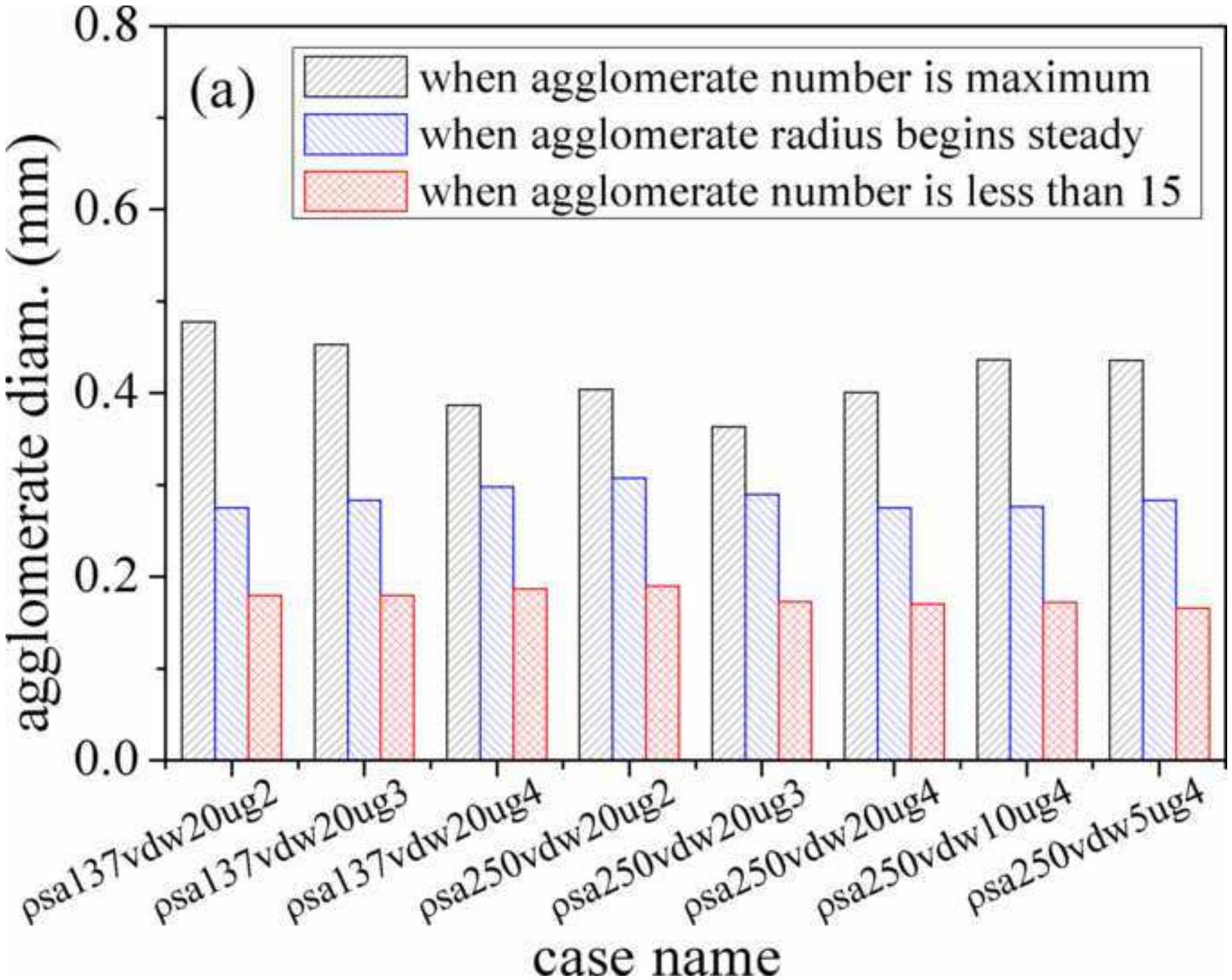

Figure 9b
Click here to download high resolution image

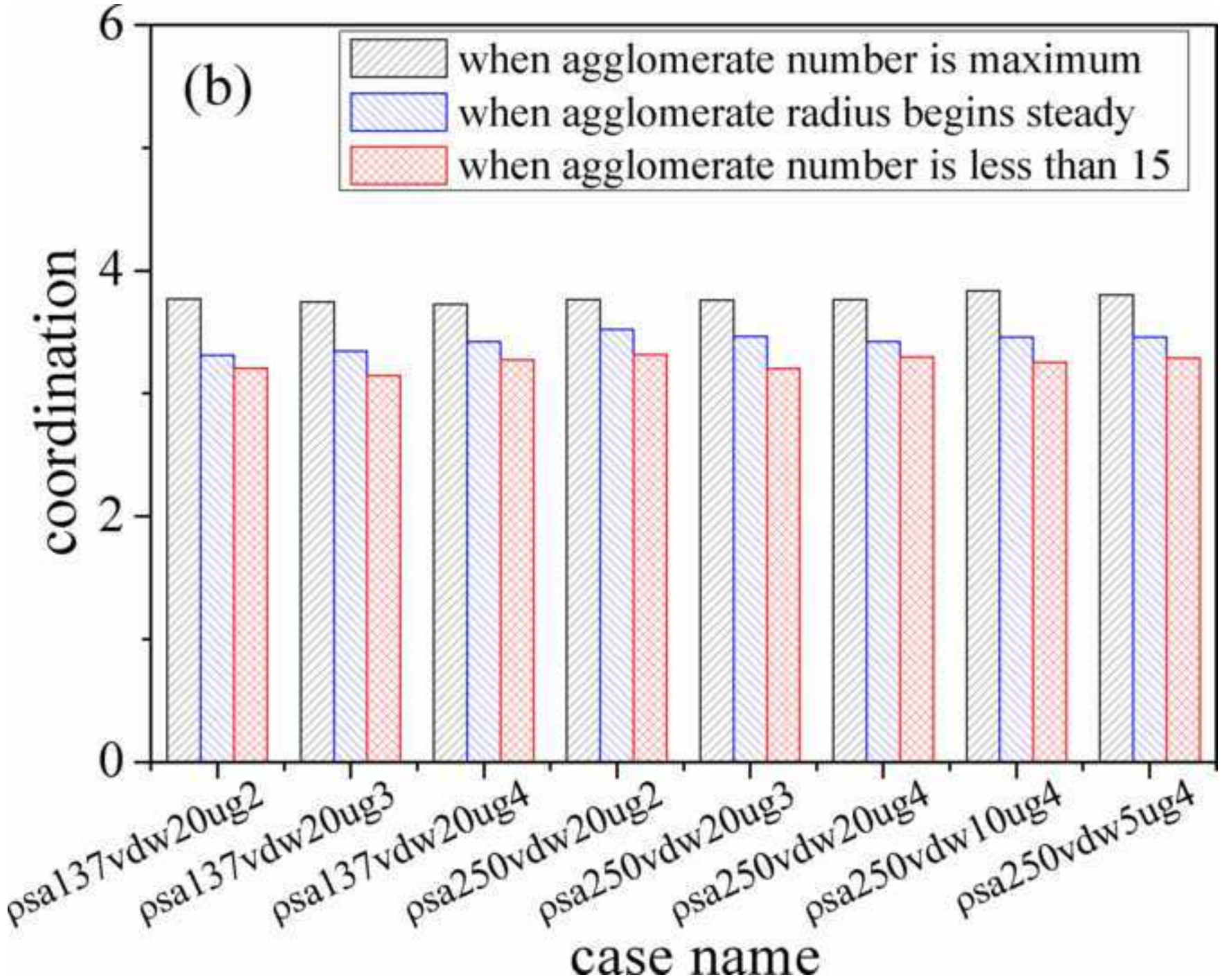

Figure 9c

Click here to download high resolution image

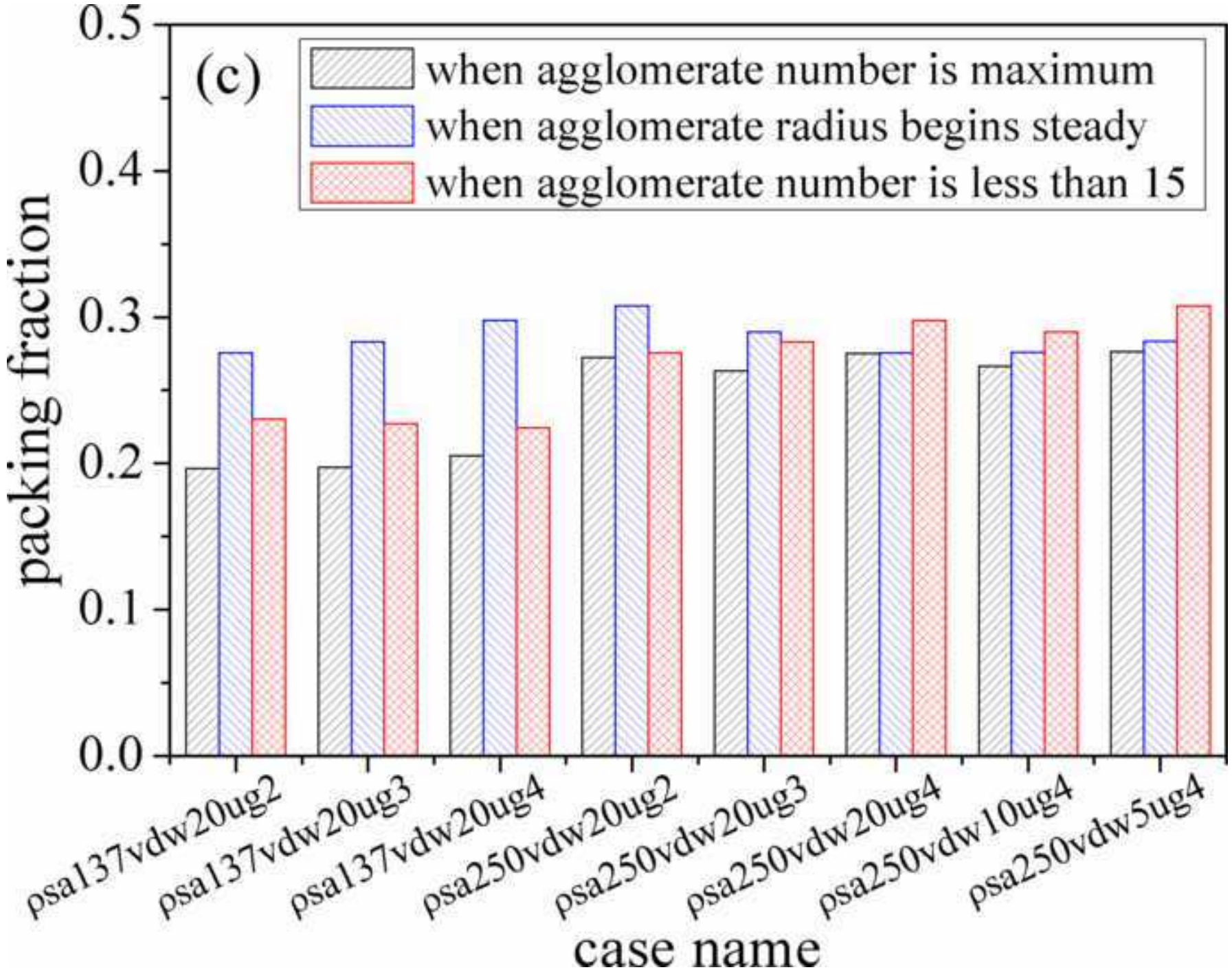

Figure 9d
Click here to download high resolution image

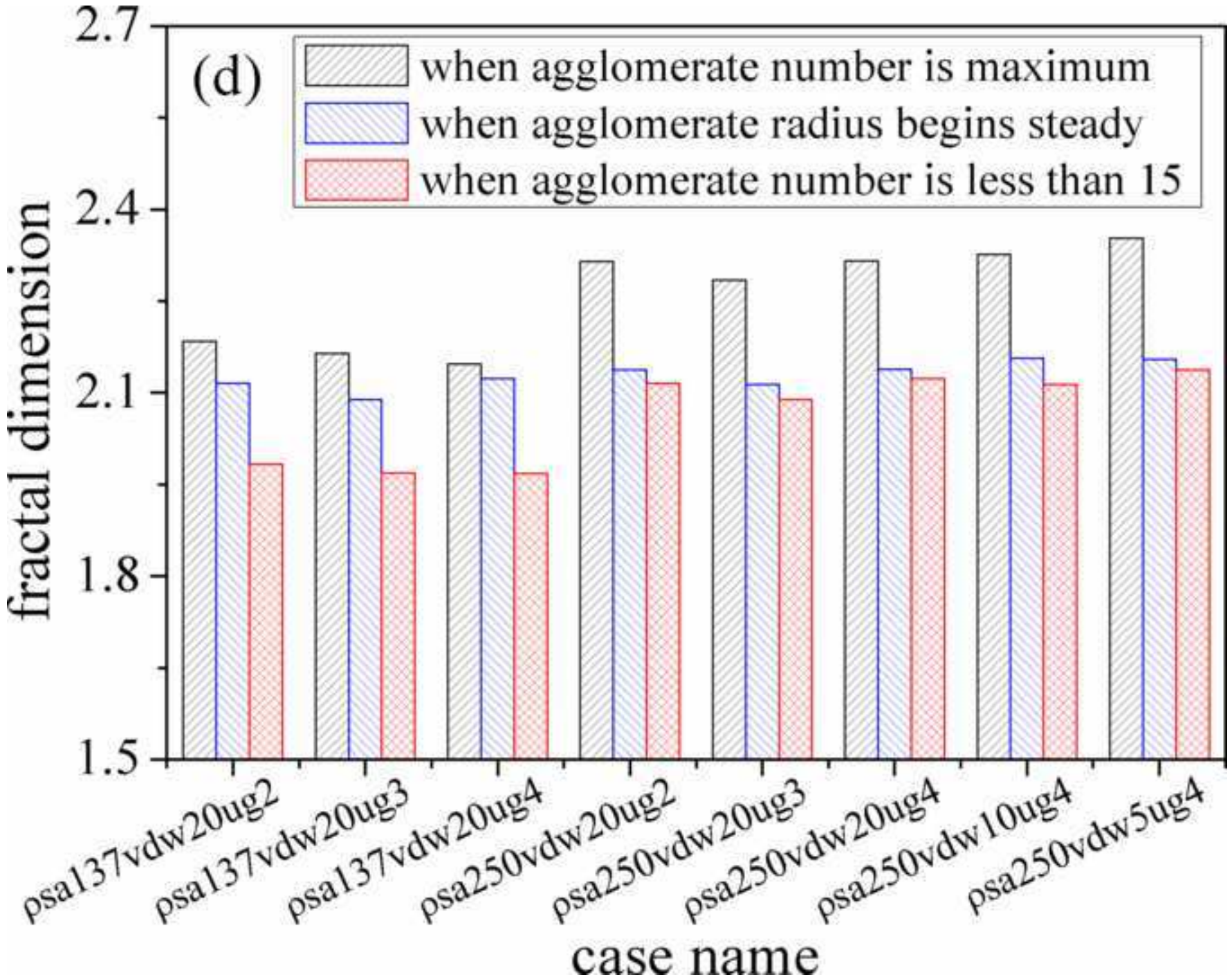

Figure 10

Click here to download high resolution image

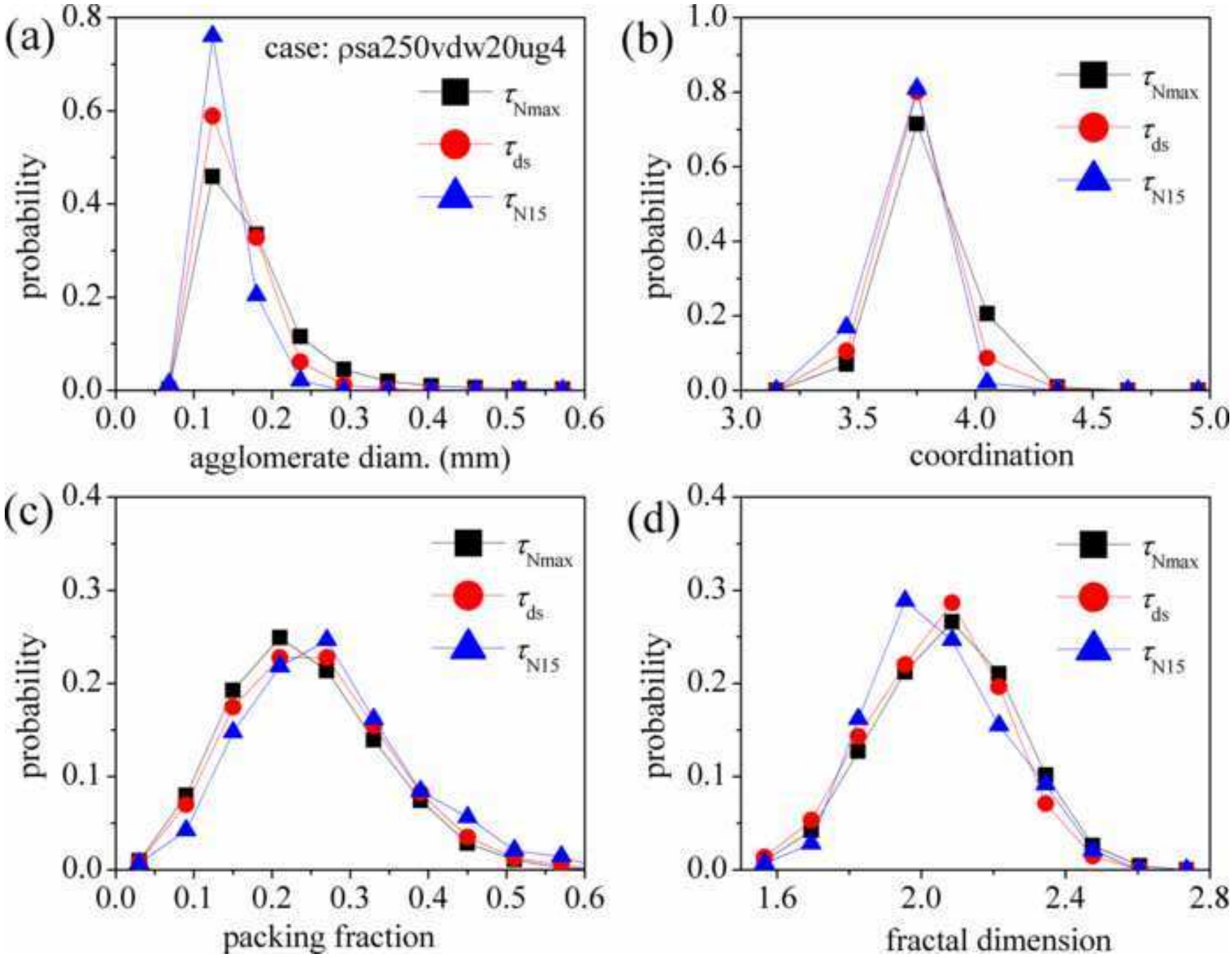

Table 1

Table 1

mass and momentum conservation equations of fluid phase

$$\frac{\partial}{\partial t}\left(\varepsilon_g \rho_g\right)+\nabla\cdot\left(\varepsilon_g \rho_g \mathbf{u}_g\right)=0 \qquad \frac{\partial}{\partial t}\left(\varepsilon_g \rho_g \mathbf{u}_g\right)+\nabla\cdot\left(\varepsilon_g \rho_g \mathbf{u}_g \mathbf{u}_g\right)=-\varepsilon_g \nabla p_g-\nabla\cdot\left(\varepsilon_g \boldsymbol{\tau}_g\right)+\mathbf{S}_\mathbf{p}+\varepsilon_g \rho_g \mathbf{g}$$

$$\varepsilon_g=1-\sum_{n=1}^{N_p} V_{pn}\Big/V_{cell} \qquad \mathbf{S}_\mathbf{P}=-\frac{1}{V_{cell}}\sum_{n=1}^{N_p}\frac{V_a\beta}{\left(1-\varepsilon_g\right)}\left(\mathbf{u}_g-\mathbf{v}_\mathbf{p}\right)\cdot\xi \qquad \xi \text{ drag force scale factor}$$

motion equations of each particle

$$m_a\frac{d\mathbf{v}_a}{dt}=-V_a\nabla p_g+\mathbf{F}_d\,\xi+m_a\mathbf{g}+\sum_{b=1}^{N}\left(\mathbf{F}_{ab,n}+\mathbf{F}_{ab,t}\right) \qquad I_a\frac{d\mathbf{w}_a}{dt}=\sum_{b=1}^{N}\left(R_b\mathbf{n}_{ab}\times\mathbf{F}_{ab,t}\right)$$

$$\mathbf{F}_d=\frac{V_a\beta}{\left(1-\varepsilon_g\right)}\left(\mathbf{u}_g-\mathbf{v}_\mathbf{p}\right)$$

Wen&Yu drag coefficient

$$\beta=\frac{3}{4}C_D\frac{\rho\left|\mathbf{u}_g-\overline{\mathbf{v}_\mathbf{p}}\right|\left(1-\varepsilon_g\right)}{d_p}\varepsilon_g^{-2.7} \qquad Re=\rho_g\varepsilon_g\left|\mathbf{u}_g-\overline{\mathbf{v}_\mathbf{p}}\right|d_p\Big/\mu_g$$

adhesive particle contact model

$\mathbf{F}_{ab,n}=-\mathrm{F_n}(d)\mathbf{n}_\mathbf{ab}-\eta_n\mathbf{v}_{ab,n}$ $\mathrm{F_n}(d)$ includes cohesive force

during the approach stage $\mathrm{F_n}(d)=0$ $d(t)>H_0$ H_0 minimal separation distance

during the initial loading stage $\mathrm{F_n}(d)=k_{n,load}\delta_n-F_{vdw,0}$

during the reloading and unloading stages $\mathrm{F_n}(d)=\begin{cases}k_{n,unload}(\delta_n-\delta_p)-F_{vdw,0} & \mathrm{F_n}\geq f_{ad,\min}\\(1-x_1)(-F_{vdw,0}-F_{bond,0})+x_1 f_{ad,\min} & \mathrm{F_n}<f_{ad,\min}\end{cases}$

$F_{bond,0}$ other cohesive forces, e.g. the hydrogen bond force. $F_{bond,0}=0$ in this paper

maximum magnitude of the cohesive force $f_{ad,\min}=(\delta_0/d_{p,NP}+1)(-F_{vdw,0}-F_{bond,0})$

$d_{p,NP}$ primary nanoparticle size; $x_1=d/\delta_{ad,\min}$, linear interpolation fraction between $d=0,\delta_{ad,\min}$

permanent plastic deformation $\delta_p=(1-k_{n,load}/k_{n,unload})\delta_{\max}$

If $\mathbf{F}_{ab,t}>\mu_f\left|\mathbf{F}_{ab,n}\right|$ then $\mathbf{F}_{ab,t}=-\mu_f\left|\mathbf{F}_{ab,n}\right|\mathbf{t}_{ab}$, and reset $\boldsymbol{\delta}_t=\mathbf{F}_{ab,t}/k_t$

relative velocity, direction unit vector, and overlap

$$\mathbf{v}_{ab}=\left(\mathbf{v}_a-\mathbf{v}_b\right)+\left(R_a\mathbf{w}_a+R_b\mathbf{w}_b\right)\times\mathbf{n}_{ab} \qquad \mathbf{v}_{ab,n}=\left(\mathbf{v}_{ab}\cdot\mathbf{n}_{ab}\right)\mathbf{n}_{ab} \qquad \mathbf{v}_{ab,t}=\mathbf{v}_{ab}-\mathbf{v}_{ab,n}$$

$$\mathbf{n}_{ab}=\left(\mathbf{r}_b-\mathbf{r}_a\right)\Big/\left|\mathbf{r}_b-\mathbf{r}_a\right| \quad \mathbf{t}_{ab}=\mathbf{v}_{ab,t}\Big/\left|\mathbf{v}_{ab,t}\right|$$

$$\delta_n=R_a+R_b-\left|\mathbf{r}_a-\mathbf{r}_b\right| \qquad \boldsymbol{\delta}_t'=\boldsymbol{\delta}_{t0}+\mathbf{v}_{ab,t}\,\Delta t \qquad \boldsymbol{\delta}_t=\boldsymbol{\delta}_t'-\left(\boldsymbol{\delta}_t'\cdot\mathbf{n}_{ab}\right)\mathbf{n}_{ab}$$

damping coefficient

$$\eta_n=2\sqrt{m_{ab}k_n}\,\ln e_{vis}\Big/\sqrt{\pi^2+\ln^2 e_{vis}} \qquad \eta_t=2\sqrt{m_{ab}'k_t}\,\ln e_{vis}\Big/\sqrt{\pi^2+\ln^2 e_{vis}}$$

Table 2

Table 2

case No.	case abbreviation	ρ_{sa}(kg/m^3)	description Bo_{vdw} ($F_{vdw,0}$, nN)	u_g(cm/s)
1	ρsa137vdw20ug2	137	20 (0.9)	2
2	ρsa137vdw20ug3	137	20 (0.9)	3
3	ρsa137vdw20ug4	137	20 (0.9)	4
4	ρsa250vdw20ug2	250	20 (1.7)	2
5	ρsa250vdw20ug3	250	20 (1.7)	3
6	ρsa250vdw20ug4	250	20 (1.7)	4
7	ρsa250vdw10ug4	250	10 (0.8)	4
8	ρsa250vdw5ug4	250	5 (0.4)	4